2012

Micro-Raman Imaging and Hyperspectral Analysis of Tibiotarsi from Chick Embryos Exposed to Sublethal Doses of Platinum Group Metals

Adam Christopher Stahler
Wright State University

Repository Citation

Stahler, Adam Christopher, "Micro-Raman Imaging and Hyperspectral Analysis of Tibiotarsi from Chick Embryos Exposed to Sublethal Doses of Platinum Group Metals" (2012). *Browse all Theses and Dissertations*. 624.
https://corescholar.libraries.wright.edu/etd_all/624

MICRO-RAMAN IMAGING AND HYPERSPECTRAL ANALYSIS OF TIBIOTARSI FROM CHICK EMBRYOS EXPOSED TO SUBLETHAL DOSES OF PLATINUM GROUP METALS

A thesis submitted in partial fulfillment of the
requirements for the degree of
Master of Science

By

ADAM CHRISTOPHER STAHLER
B.S., Wright State University, 2010

2012
Wright State University

WRIGHT STATE UNIVERSITY

GRADUATE SCHOOL

August 18, 2012

I HEREBY RECOMMEND THAT THE THESIS PREPARED UNDER MY SUPERVISION BY Adam Christopher Stahler ENTITLED Micro-Raman imaging and hyperspectral analysis of tibiotarsi from chick embryos exposed to sublethal doses of platinum group metals BE ACCEPTED IN PARTIAL FULFILMENT OF THE REQUIREMENTS FOR THE DEGREE OF Master of Science.

Ioana E.P. Sizemore, Ph.D.
Thesis Director

David A. Grossie, Ph.D.
Chair, Department of Chemistry

Committee on
Final Examination

Ioana E.P. Sizemore, Ph.D.

David A. Dolson, Ph.D.

Paul G. Seybold, Ph.D.

Andrew Hsu, Ph.D.
Dean, Graduate School

ABSTRACT

Stahler, Adam Christopher. M.S., Department of Chemistry, Wright State University. 2012. Micro-Raman imaging and hyperspectral analysis of tibiotarsi from chick embryos exposed to sublethal doses of platinum group metals.

Platinum group metals (PGMs), *i.e.*, Pd, Pt and Rh, are found at pollutant levels in the environment. PGMs accumulate in plant and animal tissues, and little is known about their toxicity. Our previous studies have shown that chick embryos exposed to 1.0 mL PGM solutions of 5.0 ppm (LD_{50}) and higher exhibited severe skeletal deformities. This work hypothesized that 1.0 ppm sublethal doses of PGMs would negatively impact the mineralization process in tibiotarsi. One milliliter of 1.0 ppm of Pd(II), Pt(IV), Rh(III) aqueous salt solutions and a PGM-mixture were injected into the air sac of the eggs on the 7th and 14th day of incubation. Control groups were also included. On the 20th day, embryos were sacrificed to analyze the PGM effects on tibiotarsi using micro-Raman imaging. Hyperspectral data analysis was performed using custom-written MatLab codes. The univariate Raman images that were created from the $\nu_1(PO_4^{3-})$ integrated areas of hydroxyapatite revealed anomalous mineral inclusions within the bone marrow cavity for the PGM-mixture treatment, and explained the observed pathological changes. The age of the mineral crystals ($\nu(CO_3^{2-})/\nu_1(PO_4^{3-})$) was found to be statistically lower for all treatments when compared to controls ($p \leq 0.05$). The abnormal mineral distribution and the younger tibiotarsi may be explained by a delay in the endochondral ossification process as a result of PGM exposure.

TABLE OF CONTENTS

1 INTRODUCTION 1

1.1 Platinum group metals 1

1.2 Previous research & results 3

1.3 Experimental description 4

1.4 Hypothesis 5

1.5 Specific aims: 6

1.6 Hyperspectral data and univariate Raman images 5

1.7 The chick embryo model 6

1.7.1 Chick embryo model justification 6

1.7.2 Cartilage 7

1.7.3 Bone 8

1.7.4 Endochondral ossification process 9

2 TECHNICAL APPROACH 12

2.1 *In Ova* injections and sample collection 12

2.2 Tibiotarsi sample preparation 14

2.3 Specific aim 1 15

2.3.1 Raman spectroscopy working principle 15

TABLE OF CONTENTS (CONTINUED)

        2.3.2 Acquisition of micro-Raman maps of tibiotarsus cross-sections............. 20

    2.4 Specific aim 2: Development of a custom algorithm for the construction of univariate Raman images.. 21

    2.5 Specific aim 3 22

        2.5.1 Age of mineral crystals in literature.. 22

        2.5.2 Development of a custom algorithm for the estimation of the age of mineral crystals 23

        2.5.3 Statistical analysis.. 24

3 RESULTS AND DISCUSSION 26

    3.1 Analysis of the gross morphology of tibiotarsus cross-sections........................... 26

    3.2 Analysis of the micro-Raman univariate images of tibiotarsus cross-sections..... 27

    3.3 Estimation of the age of mineral crystals of tibiotarsus cross-sections 49

4 CONCLUSIONS 52

5 REFERENCES... 54

6 ADDENDA.. 59

    6.1 Parsing micro-Raman map data 60

    6.2 Concatenating incremental micro-Raman map data 60

    6.3 Univariate Image Construction 63

TABLE OF CONTENTS (CONTINUED)

6.4 Creation of logical matrix 68

6.5 Age of mineral crystals calculation.. 70

7 CURRICULUM VITAE.. 75

LIST OF FIGURES

Figure 1.1: Left) Chick embryo exposed to 5.0 ppm of Pt showing an abnormal skull protrusion. **Right)** Deformed rib cage in chick exposed to 10.0 ppm of Rh resulting in the development of abdominal organs outside the body. 4

Figure 2.1: Typical Raman energy diagram. 16

Figure 2.2: Photo of theLabRamHR micro-Raman system (Horiba Jobin Yvon Inc.). .. 20

Figure 3.1: Left) Raman spectrum of the paraffin embedding material. Inset shows the Raman spectrum in the 1000 cm^{-1} – 1250 cm^{-1} spectral range. **Right)** Raman spectrum of tibiotarsus tissue obtained from a vehicle-treated embryo. Only the peaks assigned to vibrational modes of cartilage tissue were labeled. Both Raman spectra (**Left and Right**) were collected using a 632.8 nm excitation source, 3 s acquisition time and 2 cycles. 28

Figure 3.2: Top) Optical image of a no injection control tibiotarsus cross-section collected using the 10x objective of the confocal Raman microscope. The red inset (15 μm x 1600 μm) represents the area that was micro-Raman mapped. **Bottom)** Micro-Raman image of this area.. 35

LIST OF FIGURES (CONTINUED)

Figure 3.3: Top) Optical image of a second no injection control tibiotarsus cross-section collected using the 10x objective of the confocal Raman microscope. The red inset (15 μm x 1500 μm) represents the area that was micro-Raman mapped. **Bottom)** Micro-Raman image of this area... 36

Figure 3.4: Top) Optical image of a vehicle control tibiotarsus cross-section collected using the 10x objective of the confocal Raman microscope. The red inset (15 μm x 1364 μm) represents the area that was micro-Raman mapped. **Bottom)** Micro-Raman image of this area (Micro-Raman map data collected by Monahan (2010)). 37

Figure 3.5: Top) Optical image of duplicate vehicle control tibiotarsus cross-section collected using the 10x objective of the confocal Raman microscope. The red inset (15 μm x 1500 μm) represents the area that was micro-Raman mapped. **Bottom)** Micro-Raman image of this area... 38

Figure 3.6: Top) Optical image of a Pd-treated tibiotarsus cross-section collected using the 10x objective of the confocal Raman microscope. The red inset (15 μm x 2332 μm) represents the area that was micro-Raman mapped. **Bottom)** Micro-Raman image of this area (Micro-Raman map data collected by Monahan (2010)). 39

Figure 3.7: Top) Optical image of a second Pd-treated tibiotarsus cross-section collected using the 10x objective of the confocal Raman microscope. The red inset (15 μm x 1480 μm) represents the area that was micro-Raman mapped. Bottom) Micro-Raman image of this area. 40

LIST OF FIGURES (CONTINUED)

Figure 3.8: Top) Optical image of a Pt-treated tibiotarsus cross-section collected using the 10x objective of the confocal Raman microscope. The red inset (15 μm x 1557 μm) represents the area that was micro-Raman mapped. Bottom) Micro-Raman image of this area (Micro-Raman map data collected by Monahan (2010)). 41

Figure 3.9: Top) Optical image of a Pt-treated tibiotarsus cross-section collected using the 10x objective of the confocal Raman microscope. The red inset (15 μm x 1411 μm) represents the area that was micro-Raman mapped. Bottom) Micro-Raman image of this area. 42

Figure 3.10 Top) Optical image of a Rh-treated tibiotarsus cross-section collected using the 10x objective of the confocal Raman microscope. The red inset (15 μm x 2690 μm) represents the area that was micro-Raman mapped. **Bottom)** Micro-Raman image of this area. 43

Figure 3.11: Top) Optical image of a duplicate Rh-treated tibiotarsus cross-section collected using the 10x objective of the confocal Raman microscope. The red inset (15 μm x 2100 μm) represents the area that was micro-Raman mapped. **Bottom)** Micro-Raman image of this area (Micro-Raman map data collected by Monahan (2010)). 44

LIST OF FIGURES (CONTINUED)

Figure 3.12: Top) Optical image of a PGM-mixture-treated tibiotarsus cross-section collected using the 10x objective of the confocal Raman microscope. The red inset (15 μm x 1500 μm) represents the area that was micro-Raman mapped. **Bottom)** Micro-Raman image of this area. ... 45

Figure 3.13: Top) Optical image of a second PGM-mixture-treated tibiotarsus cross-section collected using the 10x objective of the confocal Raman microscope. The red inset (15 μm x 1943 μm) represents the area that was micro-Raman mapped. **Bottom)** Micro-Raman image of this area (Micro-Raman map data collected by Monahan (2010)). ... 46

Figure 3.14: A) Optical image (10x objective) of a chick embryo tibiotarsus exposed to the PGM-mixture. **Inset:** Optical image (100x objective) of a highly mineralized region found within the medullary cavity indicated by red inset in panel A. **B)** Univariate micro-Raman image constructed from **C)** the baseline corrected integrated area of the phosphate band. **D)** A point Raman spectrum collected from the mineralized region between 100 cm^{-1} – 2000 cm^{-1}. ... 47

Figure 3.15: Optical images of PGM-mixture treated chick embryo tibiotarsus cross-sections (10x objective) from three specimens. Optical images A) and B) show the presence of large abnormal mineral inclusions. C) Tibiotarsus cross-section show several, smaller mineral inclusions. Point micro-Raman measurements confirmed the presence of anomalous mineral inclusions (denoted by red ellipses). ... 48

LIST OF FIGURES (CONTINUED)

Figure 3.16: Quartile plot displaying the median value for the estimated age of mineral crystals. Center lines in grey boxes mark the median value. The 25th and 75th percentiles are represented by the top and bottom edges of shaded box, respectively. The whisker marks show the 10th and 90th percentiles (upper and lower marks, respectively). The number of pixels used to calculate the age of mineral crystals is denoted by *N* for each specimen. Statistical differences were detected by Kruskal-Wallis Anova on Ranks ($p \leq 0.001$) and determined by Dunn's multiple comparison tests ($p \leq 0.05$). Treatment or control values denoted with the same letter were not statistically different.. 51

LIST OF TABLES

3.1: Raman vibrational modes observed for tibiotarsus samples with their tentative assignments.. 29

A.1: Example of Micro-Raman map data as a text file (.txt). Spatial coordinates are in green, the wavenumber axis is the blue row vector, and the values in red are the Raman intensities for each pixel along the wavenumber axis.................................. 59

ACKNOWLEDGEMENTS

I would first like to thank my advisor, Dr. Ioana Sizemore, for two years of exceptional support, patience, understanding, encouragement, and guidance. Her extraordinary direction has been a significant motivating force in my life. I would also like to thank the other members of Dr. Sizemore's research group for their help in our many endeavors. I appreciate all the time we have spent together.

I would like to acknowledge Dr. Paul Seybold and Dr. David Dolson for sharing their vast wealth of knowledge and serving as my committee members. I would also like to express thanks to the Wright State University's Department of Chemistry faculty and staff. I would lastly, like to thank my mother, father, siblings and friends for their never wavering support.

1 INTRODUCTION

1.1 Platinum group metals

The elements iridium (Ir), osmium (Os), palladium (Pd), platinum (Pt), rhodium (Rh), and ruthenium (Ru) are members of the platinum group metals (PGMs). The relatively heavier element Pt is extensively used as a catalyst to reduce industrial emissions into less harmful compounds.[1] Pt, Pd and Rh are present in automobile catalytic converters where they catalyze the oxidation and reduction of exhaust emissions.[1] In 1970, the U.S. Congress passed the Clean Air Act, which required newly manufactured cars to be outfitted with catalytic converters by 1975 in order to improve air quality.[1, 2] Currently, approximately 95% of new cars and over half of existing cars worldwide are equipped with catalytic converters.[2, 3] In most new cars, three-way catalytic converters reduce nitrous oxides to diatomic oxygen and nitrogen (Pt and Rh), and catalyze the oxidation of carbon monoxide and non-combusted hydrocarbons to CO_2 (Pt and Pd).[4, 5] Secondary uses of PGMs include chemical processing, petroleum refining, the fabrication of electronic devices, dental alloys, anti-tumor/anti-cancer treatments (*e.g.*, *cis*-dichlorodiamineplatinum (II)), and jewelry.[3, 4]

The use of catalytic converters has significantly improved air quality. However, dust and particulates of Pd, Pt, and Rh are easily removed from the catalytic surface through abrasion and surface corrosion resulting in PGM deposition along roadside soils.[4-10] Recent studies on automobile emission dust showed that a single car emitted daily about 3-200 ng of Pt per m^3 of air in the form of particulates of median diameters of 50 nm to 20 μm.[6, 7] A 2001 study performed on three, moderately trafficked roadside soils surrounding South Bend, Indiana, revealed levels of Pd, Pt, and Rh between 18.0 – 31.0 ppb, 64.0 – 73.0 ppb, and 3.0 – 7.0 ppb.[9] PGM mean concentrations were found to be even higher in soil samples collected in 2004 from a major German highway (83.0 ppb for Pd, 132.0 ppb for Pt, and 20.0 ppb for Rh). [9] Pd soil concentrations as high as 440.0 ppb and Pt levels of 200.0 ppb have been reported in Perth, Australia and Pahang, Malaysia, respectively. [10, 11] These concentrations are significantly higher than the natural levels of PGMs in the earth's crust (5.0 ppb of Pt, 1.0 ppb of Pd, and 0.4 ppb of Rh).[1]

While metallic PGM particulates are considered to be biological inert, recent studies have shown that 10% - 43% of Pt emissions are water soluble.[6, 9, 12] In soluble form, PGMs can readily form complex salts with a variety of ligands (*e.g.*, halogens, cyano groups, hydroxides, and sulfur).[12] Gagnon *et al.* reported that *Daucus carota* plants uptook and bioaccumulated these complex PGM salts. Furthermore, flame atomic absorption spectroscopic analysis of the plant tissue revealed mean Pt, Pd, and Rh concentrations of 14.6 ppm, 10.2 ppm, and 0.7 ppm, respectively.[4]

Owing to these anthropogenic sources, PGM concentrations in the environment are significantly increasing. For example, Zereini *et al.* reported that Pt and Pd concentrations had increased 2-fold and 1.6-fold, respectively, over a time period of 10 years (1994 – 2004) within the same sample site.[9] This raises major concerns about PGMs toxicity to humans and animals.

Average Pd and Rh concentrations of 7.5 ± 5.4 ppb and 8.5 ± 0.8 ppb were reported in urine samples from 310 school children living in the urban and suburban areas of Rome, Italy. These samples were collected and analyzed in between 1996 and 2001, and PGM concentrations were found to be strongly correlated with traffic density.[13] Vaughan *et al.* reported that the average daily dietary intake of Pt was as high as 1.44 μg for adults in Sydney, Australia.[14] Farago *et al.* indicated that occupationally exposed precious metal workers had Pt blood concentrations of 246.0 ± 177.0 ppb. This value was approximately 90% higher than the Pt blood concentrations of non-exposed individuals.[15] Such high concentrations of Pt salts led to the development of allergic dermatitis and caused respiratory distress in occupationally exposed workers. Symptoms included but were not limited to wheezing, coughing, and shortness of breath. These symptoms are collectively termed *platinosis*.[16]

1.2 Previous research & results

Our recent studies on chick embryos exposed to varying doses of PGMs showed severe pathological, toxic and genotoxic responses.[17-19] Previous studies have revealed alarming calcium inclusions within chick embryo brain tissue following exposure to 1.0 mL of 5.0 ppm Rh. Grotesque skeletal deformities such as the brain protruding through an improperly developed skull were observed for developing chick embryos exposed to 1.0 mL of 5.0 ppm Pt concentration (identified as LD_{50}, Figure 1.1: Left). Chicks that were exposed to 1.0 mL of 10.0 ppm of Rh exhibited a lack of complete internalization of abdominal organs due to an improperly developed rib cage (Figure 1.1: Right). Earlier research conducted by Monahan (2010) found abnormal calcium inclusions and anomalous calcium content in chick embryo tibiotarsi exposed to sublethal doses of PGMs through micro-Raman spectroscopic imaging, X-ray fluorescence imaging, and flame atomic absorption spectroscopy.[18, 19]

Figure 1.1: Left) Chick embryo exposed to 5.0 ppm of Pt showing an abnormal skull protrusion. **Right)** Deformed rib cage in chick exposed to 10.0 ppm of Rh resulting in the development of abdominal organs outside the body (with permission from J.L. Monahan).[18, 19]

1.3 Experimental description

In this work, the effects of sublethal doses of PGMs (1.0 ppm) on chick embryo bone development were further investigated. This dose is near the immediately dangerous to life or health (IDLH) levels for the soluble salts of Rh (0.475 ppm) and Pt (0.501 ppm) as established by the U.S. National Institute for Occupational Safety and Health (NIOSH).[20] For Pd no IDLH value was listed. White Leghorn chick embryos were exposed to 1.0 mL of 1.0 ppm Pd, Pt, Rh, and a PGM-mixture containing 1.0 ppm of each metal. The treatments were injected into the air sac of the egg on the 7th and 14th day of incubation. The embryos were sacrificed on the 20th day. Tibiotarsi were harvested, fixed in formalin, dehydrated by an ethanol series, and embedded in paraffin on clean microscope slides. Micro-Raman spectroscopy was then used to image the morphology and chemical distribution in each tibiotarsus cross-section.[19]

1.4 Hypothesis

It was hypothesized that sublethal doses (1.0 ppm) of PGMs would negatively impact the bone mineralization process in chick embryos. The detrimental impact of PGM was assessed via micro-Raman imaging techniques and batch processing of hyperspectral data. In this regard, three specific aims were established.

1.5 Specific aims:

1. To collect duplicate micro-Raman map data on tibiotarsi cross-sections. (The first set of Raman images was obtained by Monahan (2010)).[18]
2. To develop a custom written MatLab univariate imaging algorithm for the investigation of the mineralization process in chick embryo tibiotarsus cross-sections.
3. To estimate the age of mineral crystals within tibiotarsus cross-sections by processing in MatLab the micro-Raman hyperspectral data. (The data collected by Monahan were also processed in MatLab for the first time).

1.6 Hyperspectral data and univariate Raman images

The micro-Raman maps that will be collected in this study represent a hyperspectral dataset. These hyperspectral datasets will contain tens of thousands of Raman spectra expressed as vectors for all discrete spatial points that will be mapped on the sample.[21] Raman images will then be constructed from the hyperspectral datasets by assigning a color code to a spectral feature (*e.g.*, band position, band intensity, integrated area, band ratios, *etc.*). A univariate image (*i.e.*, one variable) will be created by displaying these colors to the corresponding spatial region, from which the spectra will be obtain obtained.[21]

1.7 The chick embryo model

1.7.1 Chick embryo model justification

The National Institutes of Health (NIH) has recognized the chick embryo as a readily available, inexpensive and well-developed biological model for pharmacological and toxicological studies.[22] The study of the chick embryo model dates back to antiquity, where it was studied in order to better understand embryonic development.[22] The chick embryo is a well-accepted model in developmental biology, immunology, genetics, cancer research, cell biology, virology, and embryology. The avian model has aided the understanding of some of the most important, general concepts in vertebrate developmental biology including those related to human embryology.[23-25] Many genes in the chick embryo that are responsible for limb formation are homologous to the genes controlling limb and digit formation in humans.[26] Furthermore, the chick embryo is not classified as a vertebrate animal prior to hatching, and thus requires no specialized animal licensing.[22]

In this study, chick embryos' air sacs were injected with PGMs on days 7 and 14 of incubation. These days coincide with important biological benchmarks in the development of the chick embryo as described by Hamburger *et al.*[27] Beginning with stage 30 (*i.e.*, at day 6½ of incubation), the three major segments of the chick legs and wings are distinguishable. Both the wings and hind legs are bent at the elbow and knee joint, respectively. Nearly half a day later, at stage 31, the 1st and 2nd digits of the limbs start to develop, and the rudiment of the 5th toe is still distinct. During the developmental stages 32 – 33 (day 7½ and day 8 of incubation), the 5th toe has disappeared, all toes and digits have lengthened, and the web on the radial margin of the wing and the first digit become demarcated. By stage 40 (~ day 14 of incubation), the third toe has lengthened to 12.7 ± 0.5 mm, and the beak length from the anterior edge of the nostril to the tip is approximately 4.0 mm.[27]

1.7.2 Cartilage

The chick skeleton resembles those of other amniotes in that initially a large majority of the skeleton is laid down as hyaline cartilage, which over time becomes ossified.[28-30] This strong flexible tissue is the first step in the formation of mature long bones. Chondrocyte cells exist within the cartilage matrix, consisting primarily of the macromolecular constituent cartilage proteoglycan that is supported by several other proteins and glycoproteins. Chondrocytes are housed within small compartments in the cartilage matrix termed lacunae. Living chondrocytes fill their lacunae and as they mature their cytoplasm contains numerous fat droplets resulting in a vacuolated appearance. These cells become embedded in the cartilage matrix by the initial differentiation of chondroblasts into developing cartilage sites. Chondroblasts secrete the cartilage matrix constituents, and those that differentiate on the periphery of the developing cartilage sites compose a fibrous covering called the perichondrium.[29, 30]

Within the hyaline cartilage matrix about 40% to 70% of the dry weight is accounted for by type II collagen. Tissue fluid composes between 65% and 80% of the wet weight of the cartilage matrix. It is in this fluid that long range diffusion of essential nutrients and waste occurs. The cartilage matrix is avascular (*i.e.,* lacks capillaries); therefore, the long range diffusion is vital to the nourishment of chondrocytes.[29, 30]

Cartilage grows by two distinct methods. Interstitial growth occurs by an increase in proliferative chondrocytes, which results in an increase in production of the cartilage matrix from within. Appositional growth is due to the deposition of new matrix surface layers upon the existing cartilage matrix. Because, bone cells (osteocytes) do not divide, bone growth occurs only through appositional growth.[29]

1.7.3 Bone

Similar to cartilage, bone tissue possesses living cells within an extracellular matrix reinforced by collagen fibrils. However, bone tissue is heavily calcified, and therefore, it must be highly vascularized. Osteocytes located within the bone tissue matrix are embedded in *lacunae* similarly to chondrocytes in cartilage. Also, like cartilage tissue, bone tissue possesses a fibrous connective tissue termed the periosteum. Owing to calcification, bone is much harder and less supple than cartilage. The mineralized tissue matrix of bone also severely limits the ability of oxygen and nutrients to move through long range diffusion. In order for osteocytes to survive in this highly mineralized environment, numerous tiny *canaliculi* (*i.e.*, canals) connect individual *lacunae* that are bathed in tissue fluid. Within their lacunae, osteocytes are situated within 0.2 mm of a capillary, which is responsible for the production tissue fluid. The tissue fluid then reaches all osteocytes via the canaliculi.[29]

The bone matrix is capable of withstanding tensile stresses (*e.g.*, bending, twisting, compression, and stretching) due to the presence of type I and type V collagen. Approximately 90% of the organic component of bone is collagen with type I being the most abundant. Only about 25% of the bone matrix is water, while nearly 70% of the wet weight of bone is the bone mineral, hydroxyapatite ($Ca_{10}(PO_4)_6 \cdot (OH)_2$). Prior to the calcification of the organic matrix within bone, the tissue is named osteoid tissue or prebone. It is only when the calcium and phosphate ions reach the necessary levels does calcium phosphate deposition occur.[30]

1.7.4 Endochondral ossification process

There exist four cell types within the cartilage/bone matrix. Osteoprogenitor (*i.e.*, osteogenic) cells are located in areas that are highly vascularized, and differentiate into osteoblasts and osteoclasts. Ostegenic cells that differentiate in avascular regions give rise to chondroblasts. The organic components of the bone matrix are synthesized and secreted by the nondividing osteoblasts cells. Osteoblasts also play roles in the process of matrix calcification and bone resorption. Osteocytes are smaller than osteoblasts, and are the result of the final stage of maturation in the bone cell lineage. Osteoclasts are large, mobile, nondividing cells that resorb excess and substandard or weakened bone matrix during bone growth and repair.[29]

During the prenatal endochondral ossification, embryonic mesenchymal stem cells congregate and differentiate into chondroblasts that define the site of the future long bones, which make up the appendicular and axial skeleton. The chondroblasts produce the hyaline cartilage matrix and a peripheral perichondrium is developed. The cartilage precursor of the long bone continues to enlarge through appositional and interstitial growth mechanisms.[29, 30] Ossification begins in the diaphysis (*i.e.*, the midsection of long bone shafts) where the ends of long bones (*i.e.*, epiphyses) are made of hyaline cartilage. Long bone longitudinal growth occurs through interstitial growth of the epiphyses.[29, 30] The cartilage tissue of the epiphyses located next to the diaphysis then subsequently undergoes ossification.[29] In the diaphysis of the model, chondrocytes become hypertrophic and hydroxyapatite is deposited in the matrix between their lacunae.[29, 30] Next, apoptotic pathways result in chondrocyte death and numerous capillaries vascularize the perichondrium (*i.e.*, angiogenesis).[30] This allows for the differentiation of osteogenic cells near the capillaries, which constitutes the periosteal bud.[29, 30] Osteoprogenitor cells differentiate into osteoblasts within this primary ossification center, and secrete the bone matrix on the remains of the calcified cartilage tissue.[29] Initially the formed bone is cancellous bone (*i.e.*, spongy bone that is less dense than compact bone tissue) but, later the cancellous bone within the inner regions of the diaphysis is resorbed by osteoclasts, resulting in a medullary cavity.[29, 30]

The tibiotarsus is analogous to the tibia of other vertebrates. However, in *aves,* fusion of the tibia occurs with the proximal bones of the tarsus.[31] In chick embryos, the precartilaginous precursors of the femur, tibia, and fibula are formed around day 5 of incubation.[28] The tibiotarsus model from the mesenchymal stem cells appears early in day 6, becomes chondrified later that day, and begins ossification shortly afterward.[28, 29] The medullary cavity starts to form at day 8th and ossification is complete by the 11th week after hatching.[28] Disruptions in the ossification process and the appearance of anomalous mineral inclusions within cartilaginous tissue would impede long rang diffusion. Furthermore, abnormal, insoluble calcium salt inclusions would have direct consequences upon the vascularization of the perichondrium during ossification and would result in improperly vascularized mature bone tissue.

2 TECHNICAL APPROACH

2.1 *In Ova* injections and sample collection

White leghorn strain fertile specific pathogen-free avian supply eggs (SPAFAS) were obtained from Charles River Laboratories, Wilmington, MA. The air sac pole of each egg was located by candling, and was disinfected with 70% isopropanol. While being careful to leave the internal membranes intact, a 1.0 mm in diameter hole was created in the exterior eggshell of the air sac pole with a rotary drill. Clear medical tape was used to seal the holes in order to prevent contaminants from entering the eggs.[19]

Embryos were placed in a forced air incubation chamber (G.Q.F.MFG CO., Model 1502) at a temperature of $38 \pm 1^{o}C$ with relative humidity of 50-55% for 20 days (hatching occurs on day 21). To ensure equal temperature and humidity exposure, an automatic turner inside the incubation chamber rotated the embryos every 4 hours. This simulated the natural hen behavior during egg incubation. The first 24 hours in the incubator were considered to be the 1st day of ova development. On the 4th day of incubation, the embryo's development in each egg was established by candling.[19]

Water-soluble PGM salts of Pt(IV) ($H_2[PtCl_6]\cdot 6H_2O$), Pd(II) ($PdCl_2$), and Rh(III) ($RhCl_3$) were acquired as high grade aqueous solutions in 10% HCl from SPEX-CertiPrep, Inc. (1,000 mg L^{-1}). PGM concentrations were obtained by dilution in sterile phosphate-buffered saline solution (1x PBS solution, NERL Thermo Scientific). The pH of the solution was adjusted to 7.2 using 0.1 N HCl and NaOH. Solutions were filtered using a 0.22 µm filter (Fisher Scientific). The following treatments were then administered per each group of 10 embryos: 0.0 ppm control (no injection), PBS control solution containing HCl or NaOH (vehicle injection), 1.0 mL of 1.0 ppm of Pt, 1.0 mL of 1.0 ppm of Rh, 1.0 mL of 1.0 ppm of Pd, and a 1.0 mL PGM-mixture containing 1.0 ppm of each metal, were injected into the egg air sac under sterile conditions on the 7th and 14th day of incubation (*i.e.,* the two benchmark stages of the *ova* development discussed in 1.6.1).[27] This permitted the PGMs to cross the internal membrane of the embryo through diffusion. The PBS, pH adjusted solution without the addition of PGMs was used as a vehicle control (*i.e.*, the delivery medium of the PGM treatments). Because all three PGMs (*i.e*, Pd, Pt , and Rh) are often found together in the environment, a PGM-mixture treatment was established. The holes were then resealed using clear medical tape. Embryonic development was monitored *in Ova* by candling 24 hours post injection according to the Hamburger and Hamilton Normal Table.[19, 27]

On the 20th day of incubation, all treated and control embryos were sacrificed by cervical decapitation. At this stage 45, the embryo is fully developed and prepared to hatch.[27] In order to determine possible external and skeletal abnormalities; a gross visual examination was performed. Tibiotarsi from each treatment group and controls were harvested. Muscle and other soft tissues were removed. Tibiotarsus samples were then rinsed in cold 1x PBS to remove excess blood at room temperature.[19]

2.2 Tibiotarsi sample preparation

Tibiotarsus samples were stored in 10% phosphate buffered formalin solution (Fisher Scientific) for 7 days. This process fixed the tissue and prevented petrification and cellular lysis. Whole tibiotarsi were then dehydrated by a series of ethanol immersions (70%, 95%, and absolute), each lasting 45 min. An additional 45-minute absolute ethanol immersion completed the tibiotarsi dehydration. Following dehydration, a fresh clearing agent (Protocol® Safeclear™ (petroleum distillates, hydrotreated light), Fisher Scientific) was used to wash the tissues (two times for 45 min). Finally, the tissues were placed into pre-labeled plastic peel-away molds and embedded in freshly melted paraffin wax (Richard-Allan Scientific). Tibiotarsi were then placed for 45 min at 60°C in an oven in order to allow paraffin to intercalate into the empty spaces within the tissue. The samples were then allowed to cool to room temperature overnight.[19]

An adhesive solution of albumin and glycerin in a 1:1 volume ratio was freshly prepared, filtered, and shaken occasionally for 2-3 days. A few drops of formalin were added to this mixture to prevent fungal growth, and the adhesive solution was refrigerated until use.[19]

Tibiotarsi slides preparation began with the sectioning of the cooled tissue samples into ribbon slices of 3 µm thickness using a Leica 2355 Microtome. To keep the cut sections clean, the blades were changed every third section. Pre-cleaned glass microscope slides were coated with the adhesive solution. Tibiotarsus cross-sections were then mounted on the coated microscope slides with the shiny side of paraffin facing the glass. The microscope slides were placed on a warming plate overnight to facilitate the albumen coagulation onto the tissue sections. The prepared slides were then stored in a clean dry place prior to the micro-Raman measurements.[19]

2.3 Specific aim 1

2.3.1 Raman spectroscopy working principle

Raman spectroscopy is a widely used analytical tool that possesses molecular fingerprinting capabilities. Upon sample irradiation with monochromatic light, the incident radiation may be elastically or inelastically scattered. The large majority of these photons are elastically backscattered at the same energy as the incident radiation (Rayleigh scattering). However, approximately 1 in 10^6 photons experience inelastic scattering. During the inelastical backscattering process, photons loss or gain energy upon collision with the molecules. As a result, the backscattered photons have lower (*i.e.,* Stokes) or higher frequencies (*i.e,* anti-Stokes), respectively. For specific molecules, the Stokes and anti-Stokes lines produce unique spectral profiles. Nowadays, the most common source of monochromatic radiation used in Raman spectroscopy comes from lasers. Since, the Raman effect is relatively weak the use of lasers that produce highly monochromatic and very intense radiation aid in the acquisition of Raman spectra.[32 -34]

The Raman energy diagram in Figure 2.1 shows that when incident laser light (ν_L) collides with molecules, molecular energy is raised from the ground state ($\nu = 0$) or the 1st vibrational excited state ($\nu = 1$) to virtual excited states, where the energy differences between the lower states and the corresponding excited states are equal to the energy of the incident radiation. Following this excitation, most molecules return to their original state by emitting a photon of energy equal to the incident radiation (*i.e.* Rayleigh, $\nu_L = \nu_R$). A much smaller percentage of the molecules excited to the virtual state relax to the first excited vibrational/rotational molecular state by emitting a photon of lower energy (*i.e.*, the Stokes lines, ν_s). For molecules starting in the 1st excited vibrational state that relax to the ground state the backscattered photons possess greater energy (*i.e.*, anti-Stokes, ν_A). The frequency shifts of the inelastically backscattered radiation relative to the incident radiation give a direct measure of the vibrational frequencies of the molecule (ν_i). [32-34]

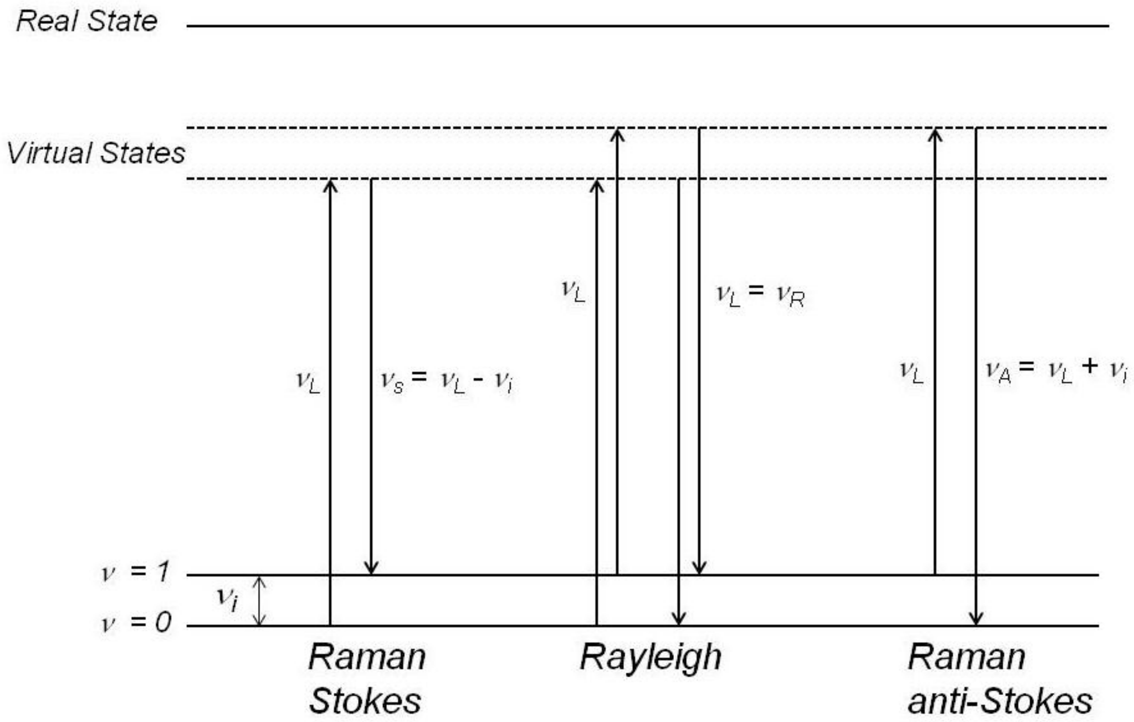

Figure 2.1: Typical Raman energy diagram. [32]

As a result of the interaction between molecules and an incident electric field with intensity (E), a dipole moment (μ_{ind}) is induced in the molecules with a magnitude

$$\mu_{ind} = \alpha E \tag{1}$$

where α is the molecular polarizability. The incident E field oscillates with the angular frequency of the incident radiation (ω_L)

$$E = E_L \cos(\omega_L t) \tag{2}$$

where E_L is the amplitude of the wave function and t is time. [32-34]

Moreover, the induced molecular dipole will also oscillate at this frequency, and according to classical EM theory any oscillating dipole will radiate energy. However, molecular polarizability is not constant for molecules in motion. This can be understood classically as the change in the electron distribution due to vibrations of nuclei within the molecule. Polarizability for a diatomic molecule can be modeled by the truncated power series in the vibrational coordinate Q_i. [32-34]

$$\alpha = \alpha_0 + \left(\frac{d\alpha}{dQ_i}\right)_0 Q_i \tag{3}$$

In equation 3 the subscript zero indicates that α_0 and $(d\alpha/dQ_i)_0$ are evaluated at equilibrium position. Using the harmonic oscillator model, the vibrational coordinate Q_i for any vibrational angular frequency (ω_i) oscillates according to equation 4. [32-34]

$$Q_i = A\cos(\omega_i t) \tag{4}$$

Appropriate substitution of equation 4 into equation into 3 yields equation 5.

$$\alpha = \alpha_0 + \left(\frac{d\alpha}{dQ_i}\right)_0 A\cos(\omega_i t) \tag{5}$$

Substituting equations 5 and 3 into equation 1and substituting 2πν for ωi reveals that

$$\mu_{ind} = \left[\alpha_0 + \left(\frac{d\alpha}{dQ_i}\right)_0 A\cos(2\pi\nu_i t)\right] \cdot E_L \cos(2\pi\nu_L t) \tag{6}$$

Upon expansion and application of the product to sum trigonometric identity (cos(a)cos(b) = ½[cos(a + b) +cos(a-b)]), the induced dipole moment has the following form. [32-34]

$$\mu_{ind} = \alpha_0 E_L \cos(2\pi(\nu_L)t) + \frac{1}{2}\left(\frac{d\alpha}{dQ_i}\right)_0 E_0\left[\cos(2\pi(\nu_L + \nu_i)t) + \cos(2\pi(\nu_L - \nu_i)t)\right] \tag{7}$$

This three term equation provides the classical explanation for the Rayleigh, Stokes, and anti-Stokes lines. The ν_L in the first term represents the Rayleigh scattering, whereas the 2nd and 3rd terms represent the higher frequency anti-Stokes scattering ($\nu_L + \nu_i$) and the lower frequency Stokes scattering ($\nu_L - \nu_i$), respectively. [32-34]

However, this classical explanation fails to account for significant differences in between the intensities of the Stokes and anti-Stokes lines. According to equation 7, both bands would be of equal intensity. In reality, the lower thermal population of the 1st excited state results in anti-Stokes lines of much lower intensity. Classically the intensity of the Rayleigh and Raman lines scales to the 4th power of the incident frequency. The Boltzmann distribution of vibrational populations reveals that

$$\frac{\text{anti}-\text{Stokes intensity}}{\text{Stokes intensity}} = \frac{(\nu_L + \nu_i)^4 e^{\frac{-h\nu_i}{kT}}}{(\nu_L - \nu_i)^4} \tag{8}$$

where h is Plank's constant and k is Boltzmann's constant. [32, 34]

Classically, a vibrational mode is said to be Raman active when $(d\alpha/Q_i) \neq 0$ (*i.e.*, when there is change in polarizability). In diatomic molecules, a change in the polarizability occurs as a result of alterations in electronic structure as the distance between nuclei change. However, a quantum model treatment reveals that the intensity of the Raman effect depends upon the square of the following integral:

$$\int \psi'^* \alpha_{i,j} \psi'' dQ_i \qquad i,j = x, y, z, \tag{9}$$

where ψ' and ψ'' are the excited and ground state wavefunctions, respectively. The integral is evaluated over the molecular coordinate system Q_i. As in the classical treatment, the integral of the products in equation 9 must be non-zero in order for the mode to be Raman active. [34]

Due to Raman scattering being a two photon process, quantum mechanical selection rules are more complex than those for pure vibrational/rotational transitions. The selection rules for vibrational/rotational Raman transitions are $\Delta v = \pm 1$ and $\Delta J = 0, \pm 2$ for linear molecules, $\Delta v = \pm 1$ and $\Delta J = 0, \pm 2$ when $\Delta K = 0$, and $\Delta v = \pm 1$ and $\Delta J = 0, \pm 1, \pm 2$ when $K \neq 0$ for symmetric top molecules. K is a component of the angular momentum, J. [33]

2.3.2 Acquisition of micro-Raman maps of tibiotarsus cross-sections

Raman data and optical images were collected from tibiotarsi using a LabRamHR 800 system (Horiba Jobin Yvon, Inc.) (Figure 2.2). The 632.8 nm output of a He-Ne laser (~15.0 mW power at the sample) was used as an excitation line. The laser beam spot had a diameter of about 1 µm and was focused on the tibiotarsus samples with a high resolution confocal Raman microscope (high stability BX41) and a long working distance 100x Olympus objective (LMPlanFLN, *NA* = 0.800). The confocal hole was set at 300 µm. The backscattered Raman signal was recorded using an open electrode thermo-electric cooled CCD detector (1024x526 pixels) and a 600 grooves mm^{-1} holographic grating. The spectral resolution was 1.125 cm^{-1}.[19]

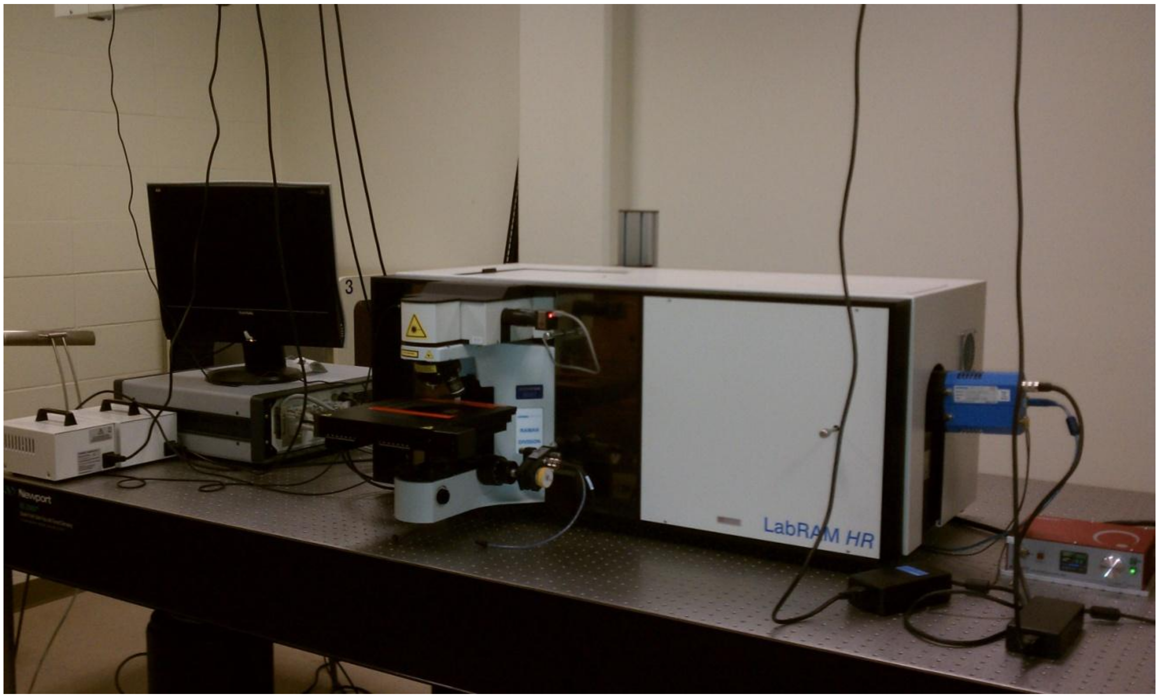

Figure 2.2: Photo of the LabRamHR micro-Raman system in 456 Oelman Hall (Horiba Jobin Yvon, Inc.).

A 15 µm wide rectangular section was selected for Raman mapping measurements on each tibiotarsus sample. The length of the map was given by the diameter of each tibiotarsus cross-section sample. Raman spectra were collected in the 100 – 2000 cm^{-1} fingerprint spectral area for every 1 µm x 1 µm spatial area (*i.e.,* pixel size). The acquisition time for each Raman spectrum was 3 seconds and the signal was averaged over 2 cycles for each pixel. These acquisition parameters allowed for the collection of spectral data with good signal to noise ratios and resulted in minimal laser damage to the samples. The autofocus option was engaged before each pixel measurement to account for the difference in height at various positions on the tibiotarsus sample and to optimize the signal-to-noise ratio. Raman maps were collected in incremental segments (15 µm width x from 150 to 300 µm length) to allow the instrument to rest and to prevent loss of data. Complete Raman maps contained between 20,000 – 40,000 spectra each. Raman data were collected using the incorporated instrument software (LabSpec v.5),[35] and were processed in MATLAB v. 7.11.0 R2010b® [36], and Origin v8.0951(B951).[37]

2.4 Specific aim 2: Development of a custom algorithm for the construction of univariate Raman images

Raman maps were collected for 60 to 120 h depending upon the cross-section diameter. The LabSpec v.5 data (.txt file format, Addenda Table A.1) was then imported into MatLab and parsed by in-house custom written codes (Addenda A.2). Incremental segment maps were concatenated as a single datablock (Addenda A.3). This facilitated the usage of complete datablocks for the construction of univariate Raman images and hyperspectral analysis algorithms. Following MatLab datablock creation, the Raman spectra of each spatial pixel were indexed as a row vector. To remove cosmic ray spikes, an 11 point median linear filter was employed to each row vector. In cartilage tissue undergoing ossification, the $\nu_1(PO_4^{3-})$ marker band represents areas rich in mineralized tissue (*i.e.*, hydroxyapatite). Therefore, a local baseline was constructed under the $\nu_1(PO_4^{3-})$ band in the 935-985 cm^{-1} spectral range for all row vectors (Addenda A.3). Next, a new vector containing only the integrated area value of the $\nu_1(PO_4^{3-})$ stretching mode for each pixel was created. These integrated area values were then translated into a new data set to reflect the actual spatial orientation of the collected micro-Raman map, and a univariate Raman image was generated. A MatLab 32 point bicubic interpolation function was utilized to reduce pixilation in the final Raman image (Figure 3.2 – 3.13).[19]

2.5 Specific aim 3

2.5.1 Age of mineral crystals in literature

Micro-Raman spectroscopy has been used for over a decade in the area of mineralized tissue research because of its powerful, non-destructive analytical properties. Literature shows that Raman spectroscopy can successfully be employed for the multiplex detection of both organic and inorganic components of cartilage/bone tissue with high spectral and spatial resolution. This allows for the assessment of significant morphological parameters. [38-42]

As previously described, the inorganic mineral component within the organic matrix of bone is hydroxyapatite ($Ca_{10}(PO_4)_6 \cdot (OH)_2$). However, as bone ages trivalent phosphate (PO_4^{3-}) and monovalent hydroxyl (OH^-) anionic sites are non-stoichiometrically substituted by carbonate ions (CO_3^{2-}). These substitutions are known as type-B and type-A carbonate substitutions with type-B carbonate being the major species. [38-42] The ratio of the baseline corrected integrated areas of the type-B CO_3^{2-} Raman band (1050 – 1090 cm^{-1}) and the $\nu_1(PO_4^{3-})$ peak (935-985 cm^{-1}) allows for the estimation of the age of mineral crystals within the bone tissue (Equation 15).

$$\text{Age of mineral crystals} = \frac{\text{Integrated area } (\nu_1(CO_3^{2-}))}{\text{Integrated area } (\nu_1(PO_4^{3-}))}^{38-43} \qquad (10)$$

More mature tibiotarsi tissue exhibit larger amounts of type B carbonate. Therefore, numerically larger calculated ratio values are indicative of an older tissue.[38-42]

2.5.2 Development of a custom algorithm for the estimation of the age of mineral crystals

The base-line corrected $\nu_1(PO_4^{3-})$ intensity values obtained with the help of the image construction algorithm were compared to the largest $\nu_1(PO_4^{3-})$ intensity within the Raman map. A new logical matrix reflecting the Raman map dimensions was then constructed using the $\nu_1(PO_4^{3-})$ peak intensity values. All pixels having a $\nu_1(PO_4^{3-})$ peak intensity value smaller than 20% of the largest $\nu_1(PO_4^{3-})$ band intensity within the entire map were set to zero, and pixels with 20 % or greater of maximum intensity were set to one. Next, the logical map containing only zeros and ones was translated into a set of row vectors and multiplied by the original, raw vectors containing the complete Raman spectral range (100-2000 cm^{-1}). This facilitated the identification and elimination of

Raman data vectors with poor signal-to-noise ratio or no phosphate content from the original, unprocessed Raman row vectors (Addenda A.4).[19]

The following three marker bands of interest: the $\nu_1(PO_4^{3-})$ stretching mode (935-985 cm^{-1}), the type B $\nu(CO_3^{2-})$ stretching mode overlapping with the paraffin C-C skeletal stretch (1050-1090 cm^{-1}), and the CH_2 deformation of paraffin (1285-1315 cm^{-1}), were base-line corrected following the procedure described in the section 2.4.[38-43] In order to subtract the C-C skeletal stretch contribution from the convoluted Raman band between 1050-1090 cm^{-1}, integrated areas were calculated for the base-line corrected paraffin CH_2 deformation mode (1285-1315 cm^{-1}) and the C-C skeletal stretch of a pure embedding paraffin sample (N = 100). The ratio of the average integrated areas (*i.e.*, Integrated area C-C skeletal stretch / Integrated area CH_2 deformation) was calculated to be 0.70 ± 0.02. Next, the integrated areas of all three bands were calculated for the micro-Raman maps of the tibiotarsi cross-sections in MatLab as previously described in section 2.4. The contribution of the paraffin C-C skeletal stretch to the integrated area of type B $\nu(CO_3^{2-})$ was subtracted for each Raman row vector. Negative values that were obtained for the integrated area of type B $\nu(CO_3^{2-})$ as a result of statistical deviations were discared. Finally, the age of mineral crystals on selected areas of the tibiotarsus cross-sections was calculated as described in equation 10 (Addenda A.5).[19]

2.5.3 Statistical analysis

Statistical analysis was performed in SigmaPlot® (v. 11).[44] The values of age of mineral crystals that were calculated in MatLab for all spatial pixels within a PGM treatment were tested for normality and equal variance (Shapiro-Wilk test). The data was non-normally distributed and did not possess equal variance ($p \leq 0.050$). As a result, a Kruskal-Wallis one way analysis of variance on ranks (*i.e.*, ANOVA) was performed to detect statistical differences between the treatment and control groups ($p \leq 0.001$), and *post hoc* Dunn's multiple comparison tests were carried out to determine statistical differences between all groups ($p \leq 0.050$).[19]

3 RESULTS AND DISCUSSION

This paragraph briefly summarizes the results presented in sections 3.1 - 3.3. Anomalous gross morphological changes were observed in the optical images of all tibiotarsi cross-sections treated with PGMs. Micro-Raman imaging in conjunction with MatLab data processing revealed an abnormal distribution of hydroxyapatite within the developing bone for all PGM treatments, and explained some of the observed morphological changes (Figures 3.2 – 3.15). Additionally, the age of mineral crystals of all tibiotarsi exposed to PGMs was found to be significantly lower than the age of the control no injection and the vehicle group (Figure 3.16).[19]

3.1 Analysis of the gross morphology of tibiotarsus cross-sections

Optical images of tibiotarsi cross-sections were acquired in duplicate using the long working distance 10x objective of the LabRam HR800 and the extended video option. A brief examination of these images shows that the gross morphologies of the tibiotarsus cross-sections in all PGM-treatment groups were markedly different from those of the control groups. However, remarkable similarities existed among the tibiotarsus cross-sections of the same group. This suggests little variability among animals receiving the same PGM treatment (Figures 3.2 – 3.13). The cancellous bone of the Pd-treated specimens was converted to dense bone to a larger degree than in the control groups, and exhibited narrow soft tissue spaces (Figures 3.6 and 3.7). The optical images of the tibiotarsus cross-sections for Pt-treatment revealed less dense perichondrial regions than in the control animals, and marrow cavities devoid of tissue (Figures 3.8 and 3.9)). Large areas of abnormal, high mineralization were observed in the developing perichondrium and the marrow cavities for the PGM mixture-treatment group (Figures 3.12 and 3.13). The tearing observed during the microtome sectioning for the Rh-treated samples was probably due to an abnormally soft tissue (Figures 3.10 and 3.11).[19]

3.2 Analysis of the micro-Raman univariate images of tibiotarsus cross-sections

First, micro-Raman spectra were collected for the pure paraffin control sample ($N = 100$) in order to determine the contribution of the embedding material to each Raman spectrum of the cartilage tissue (Figure 3.1: Left). The right panel of Figure 3.1 shows a characteristic point Raman spectrum of a tibiotarsus cross-section (vehicle control). The Raman modes associated with the inorganic and organic components of the cartilage tissue undergoing ossification are labeled. The tentative assignments of all relevant vibrational modes are summarized below in Table 3.1. These assignments are in good agreement with the Raman literature on bone tissue and paraffin. [38- 43]

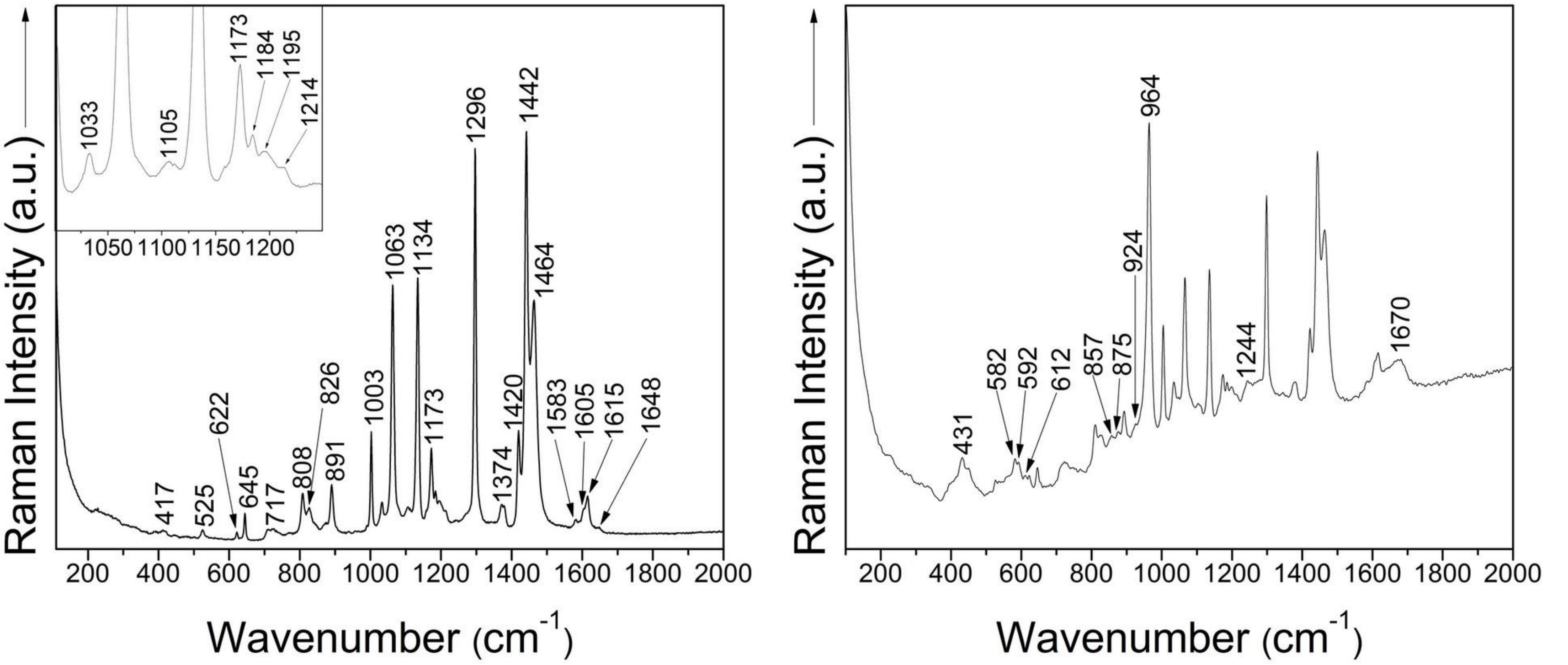

Figure 3.1: Left) Raman spectrum of the paraffin embedding material. Inset shows the Raman spectrum in the 1000 cm^{-1} – 1250 cm^{-1} spectral range. **Right)** Raman spectrum of tibiotarsus tissue obtained from a vehicle-treated embryo. Only the peaks assigned to vibrational modes of cartilage tissue were labeled. Both Raman spectra (**Left and Right**) were collected using a 632.8 nm excitation source, 3 s acquisition time and 2 cycles.[19]

Table 3.1: Raman vibrational modes observed for tibiotarsus samples and their tentative assignments.[19]

This work Raman Shift (cm^{-1})	Literature Raman Shift (cm^{-1})	Tentative assignment
417 (vw)		Paraffin
431 (m, br)	430[38-40]	Symmetric $\nu_2(PO_4^{3-})$
525 (vw)		Paraffin
582 (vw)	587[38-40]	Symmetric $\nu_4(PO_4^{3-})$
592 (vw, sh)	590[38-40]	Symmetric $\nu_4(PO_4^{3-})$
612 (vw)	609[38]	Symmetric $\nu_4(PO_4^{3-})$
622 (vw)		Paraffin
645 (w)		Paraffin
717 (vw, br)		Paraffin
808 (w)		Paraffin
826 (w,sh)		Paraffin
857(vw)	855[38]	ν(C-C) of hydroxyproline ring
875 (vw)	876[38]	ν(C-C) of proline ring
891 (m)		Paraffin
924 (vw, sh)	921[38]	ν(C-C) of proline ring
964 (vs)	~ 960 – 964[38-40]	Symmetric $\nu_1(PO_4^{3-})$
1003 (s)	1004[38, 43]	Phenylalanine, paraffin
1033 (vw)	1032 [38]	Phenylalanine, paraffin
1063 (vs)	1063[43]	Skeletal ν(CC), paraffin
1071	1071 [38-40]	ν(type B CO_3^{2-})
1105 (vw)	1103[39], 1107[40]	ν(type A CO_3^{2-}), paraffin
1134 (s)	1133[43]	ν(CC), paraffin
1173 (m)		Out of phase ν(CCC), paraffin
1184 (w,sh)		Paraffin
1195 (vw, sh)		Paraffin
1214 (vw, sh)		Paraffin
1244 (w, sh)	1245 [38]	ν(amide III)
1296 (vs)	1296[43]	CH_2 deformation
1374 (w, br)	~1375[43]	$\delta(CH_2)$, paraffin
1420 (m)	1418[43]	CH_3 deformation, paraffin
1442 (vs)	1441[43]	$\delta(CH_2)$, paraffin
1464 (s)	1463[43]	$\delta(CH_2)$, paraffin
1583 (vw)		Paraffin
1605 (vw, sh)		Paraffin
1615 (w)		Paraffin
1648 (vw, br)		Paraffin
1670 (m, br, sh)	1667[38]	Amide I (β sheet)

Abbreviations: vs – very strong, s – strong, m – medium, w – weak, vw – very weak, br – broad, sh – shoulder, ν - stretching, and δ - bending. The type-B (CO_3^{2-}) stretching mode at 1071 cm^{-1}, which overlaps with the (CC) paraffin skeletal stretch at 1063 cm^{-1}, is marked by asterisks.

After the identification of the vibrational modes characteristic to the bone tissue and the embedding material, Raman maps of tibiotarsus cross-sections were collected in duplicate for each treatment and control group. Tissue demarcated by a red rectangle in the optical images corresponds to the areas from which micro-Raman maps were recorded (Figure 3.2 – 3.13). The Raman maps of these regions were then transformed into univariate Raman images using the algorithm described in section 2.4. Regions colored in white or pink in the Raman images are indicative of high levels of mineralization, while regions highlighted in dark blue or black have little to no tissue mineralization.[19]

Figures 3.2 and 3.3 illustrate the optical images of tibiotarsus cross-sections that were obtained from two embryos of the no injection control group. The corresponding Raman images revealed moderately mineralized regions only within perichondrium. This is characteristic of a normal ossification process in chick embryos at 20 days of age.[29, 30] The optical images of the tibiotarsi in the vehicle control group (Figures 3.4 and 3.5) appeared similar in gross morphology to the no injection control specimens. The subsequent vehicle Raman images also showed mineralization of the perichondrial regions and no mineralized regions within the marrow cavity.[19] However, the duplicated vehicle map appeared to have larger areas of mineralized tissue than the other vehicle and the control samples.[19]

The developing perichondrium of one of the two tibiotarsus cross-sections in the Pd-treatment group exhibited larger areas of high mineralization compared to the control no injection and vehicle samples (Figures 3.6). Similarly mineralized regions were observed in the second Raman image for the Pd treatment when compared to the no injection and vehicle controls. Micro-Raman maps of the Pt-treated specimens revealed a less mineralized perichondrial region than the controls (Figures 3.8 and 3.9). One of the tibiotarsi of the chick embryos exposed to Rh appeared considerably less mineralized in the perichondrium compared to the controls (Figure 3.10). However, the Raman image in Figure 3.11 showed one edge lacking any mineralized tissue, while the other periphery contained a small area of unusually high phosphate content. This was most likely a consequence of the abnormally soft tissue being torn by the microtome cutting process, which resulted in indistinguishable perichondrial boundaries.[19]

Severe anomalous changes were also observed for the tibiotarsi of the PGM-mixture group. The micro-Raman image in Figure 3.13 showed an area of high mineralization within the marrow cavity of the PGM-mixture-treated tibiotarsus cross-section. The inset in Figure 3.14 (A) shows the close-up optical image (100x objective) and the corresponding Raman image of the mineralized region within the medullary cavity (B). No mineralized regions were found in the marrow cavity of the duplicated PGM-mixture treated specimen through Raman imaging (Figure 3.12). However, a large black mass similar to the one observed in the optical image of Figure 3.13 was observed in the perichondrium. These masses did not appear in the control groups or the other PGM treatments. To examine their chemical composition, micro-Raman point measurements were conducted. It was found that the inclusions consisted of abnormally large, insoluble minerals. The images were then analyzed in Image J 1.44p software.[45] The mineral crystals were found to cover up to 4 – 7 % of the total surface area in two of the tibiotarsus cross-sections in the PGM-treatment group.[19] The third cross-section exhibited numerous smaller calcium inclusions throughout both the perichondrium and the medullary cavity (Figure 3.15).[19] It should be noted that the PGM-mixture treatment consisted of 1.0 ppm of Pd, Pt, and Rh in a 1.0 mL volume. The presence of the observed calcium inclusions within this treatment may be more a result of the increased dosage and not of the inherent consequences of the PGM-mixture.

The morphological changes that were observed in the optical and Raman images of the tibiotarsus cross-sections of all PGM-treatment groups may be the result of two interrelated factors: a) the disruption of the long range diffusion process by abnormal mineral inclusions, and b) the delay in the onset of ossification due to the abnormal mineralization of the perichondrium tissue. a) As previously mentioned, the cartilage matrix containing chondrocytes is an avascular tissue, where the transport of essential waste and nutrients is facilitated through long range diffusion. The presence of abnormal, insoluble mineral inclusions within the chondrified tissue may result in the disruption of the long range diffusion processes in the cartilage tissue.[29, 30] b) It is also suspected that interferences in the ossification process may occur in the presence of abnormal mineral inclusions. Perichondrium and internal cartilage tissue interactions are essential in early long bone development.[30] The perichondrium is known to be the source of signaling pathways that regulate chondrogenesis and osteogenesis.[30] An abnormal increase in mineralization may result in the poor vascularization of the perichondrium during the initial stages of endochondral ossification. Previous studies have shown that chick embryo cartilage templates, absent of perichondrium in culture, resulted in the delay of terminal differentiation of osteogenic cells and the vascularization of hyperthropic cartilage.[30] The periosteal bud is normally highly vascularized and osteogenic cells differentiate into osteoblasts near capillaries within the matrix. Consequently, the inadequately developed, primary ossification center may result in the delay of the differentiation of osteoblasts, which are responsible for secreting the bone matrix on the remaining calcified cartilage.[29, 30]

Preventing angiogenesis in the perichondrium would also prevent the migration of osteoclasts to the developing bone tissue. The use of *cis*-dichlorodiamineplatinum (II) as an anti-tumor agent in mice has been found to result in bone marrow hypoplasia (*i.e.*, underdeveloped tissue).[46] Because, osteoclasts are derived from the monocyte/macrophage lineage of the hematopoietic progenitor cell types, underdeveloped bone marrow tissue may also be responsible for the insufficient resorption of the mineralized cartilage matrix by osteoclasts. This could also explain the observed large mineral crystals within the perichondrium and marrow cavity of the PGM-mixture-treated tibiotarsi and the abnormal mineralization for the other PGM-treated tibiotarsi. Moreover, premature mineral inclusions may also disturb the formation of canaliculi that interconnect the lacunae, which house osteocytes. This may be accompanied by a disruption of the tissue fluid responsible for osteocyte nourishment, and may result in abnormal, mature bone tissue.[29, 30]

Osteogenisis imperfect (OI) is a rare heritable disorder in which a wide range of bone fragility and low bone mass exists.[30] The bone fragility observed from OI is a result of atypical type I collagen production within the bone tissue.[30] Other recent studies have found that murine models, which were used for the study of OI, displayed abnormal mechanical properties of the collagen fibrils. As a result, significant changes in mineral crystal size and orientation were observed. Extrafibrillar and collagen-associated hydroxyapatite crystals were larger and smaller, respectively, when compared to controls.

It was also found that a higher mineral density exists within OI bone.[30] The observed large mineral inclusions within the PGM-mixture-treatment perichondrium and medullary cavity may be caused by the disruption in the type I collagen production within the developing bone tissue. This disruption could also be explained by a failure of osteoblasts differentiation in the developing bone and the subsequent production of the collagen fibrils in the bone matrix.[29, 30] Because the presence of type I collagen makes bone resistant to tensile stresses, the skeletal structural integrity of the chick embryos may be significantly compromised by atypical collagen production.[29, 30] Furthermore, the significant redistribution of hydroxyapatite observed in the all PGM -treated chick embryo tibiotarsi cross-sections could also cause sections of the developing bone to be brittle in the regions where increased amounts of mineralization occur, and soft in the areas devoid of hydroxyapatite. This observation is further supported by previous flame atomic absorption spectroscopy measurements, where % calcium levels within tibiotarsus tissue were significantly higher for the Pd-treatment (24.3 % Ca) and lower for the Pt-treatment (8.86 % Ca) than for the control no injection group (16.1 % Ca).[18, 19]

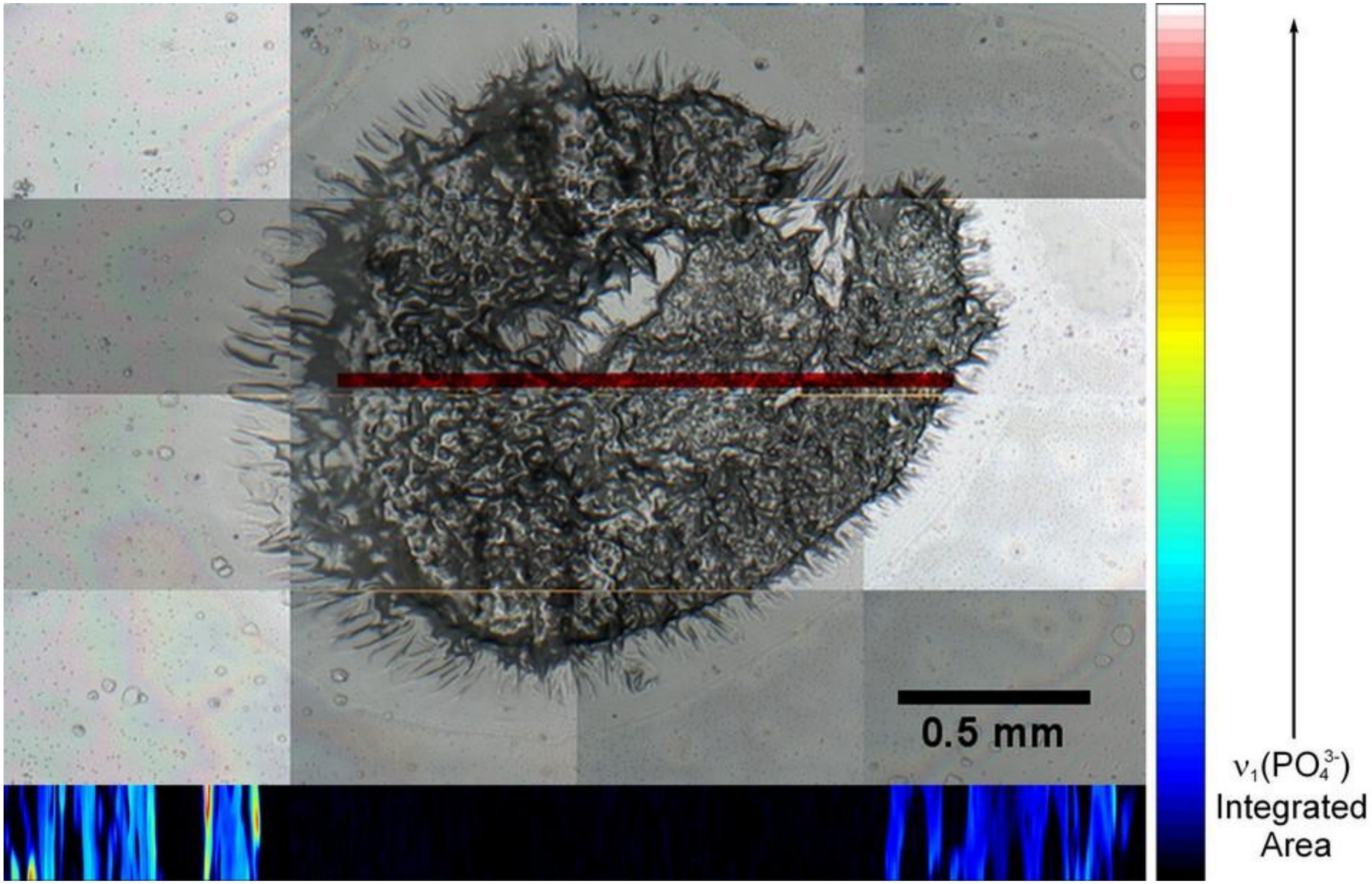

Figure 3.2: Top) Optical image of a no injection control tibiotarsus cross-section collected using the 10x objective of the confocal Raman microscope. The red inset (15 μm x 1600 μm) represents the area that was micro-Raman mapped. **Bottom)** Micro-Raman image of this area.[19]

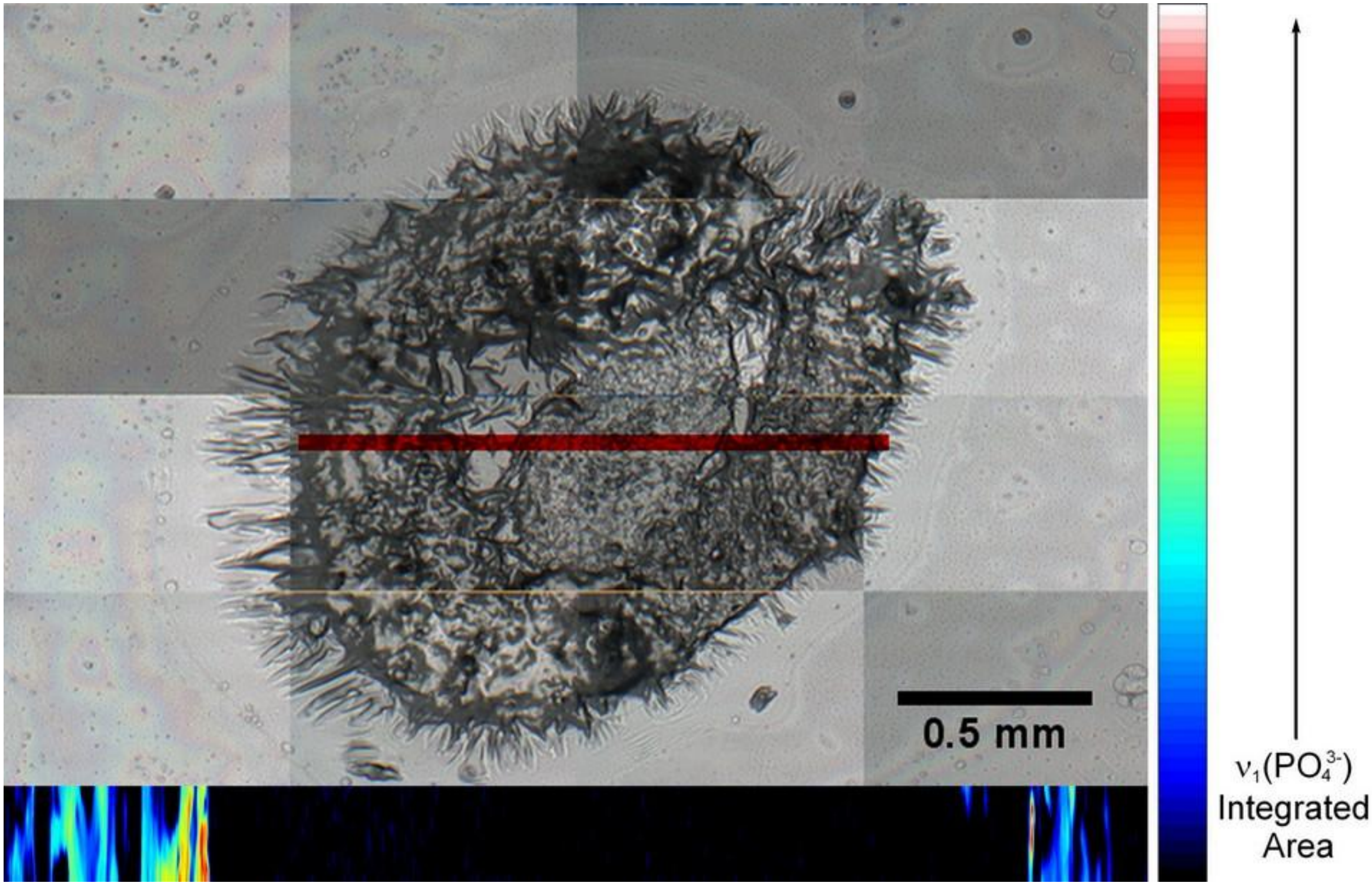

Figure 3.3: Top) Optical image of a second no injection control tibiotarsus cross-section collected using the 10x objective of the confocal Raman microscope. The red inset (15 μm x 1500 μm) represents the area that was micro-Raman mapped. **Bottom)** Micro-Raman image of this area.[19]

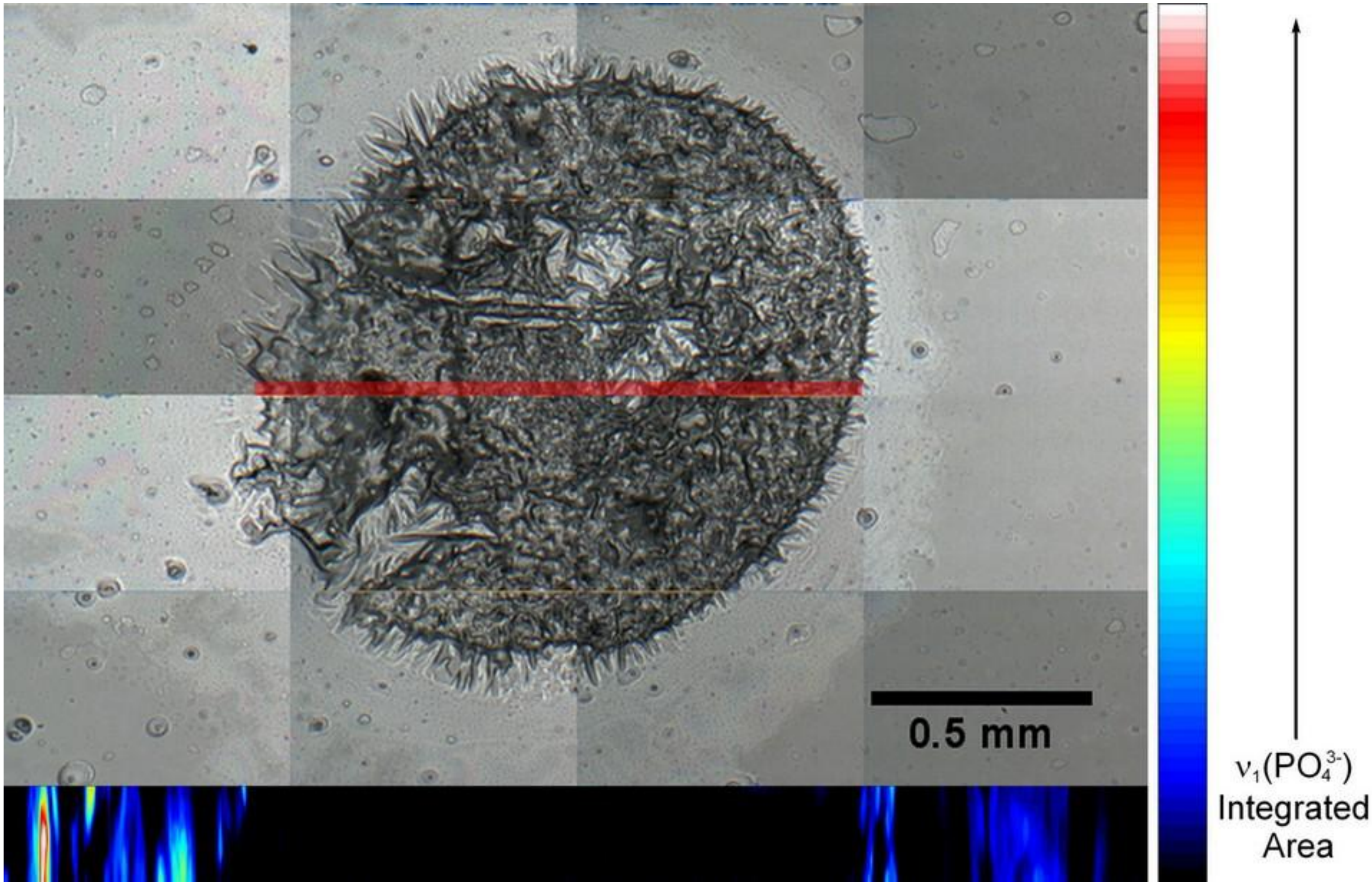

Figure 3.4: Top) Optical image of a vehicle control tibiotarsus cross-section collected using the 10x objective of the confocal Raman microscope. The red inset (15 μm x 1364 μm) represents the area that was micro-Raman mapped. **Bottom)** Micro-Raman image of this area.[43] (Micro-Raman map data collected by Monahan (2010)).[18, 19]

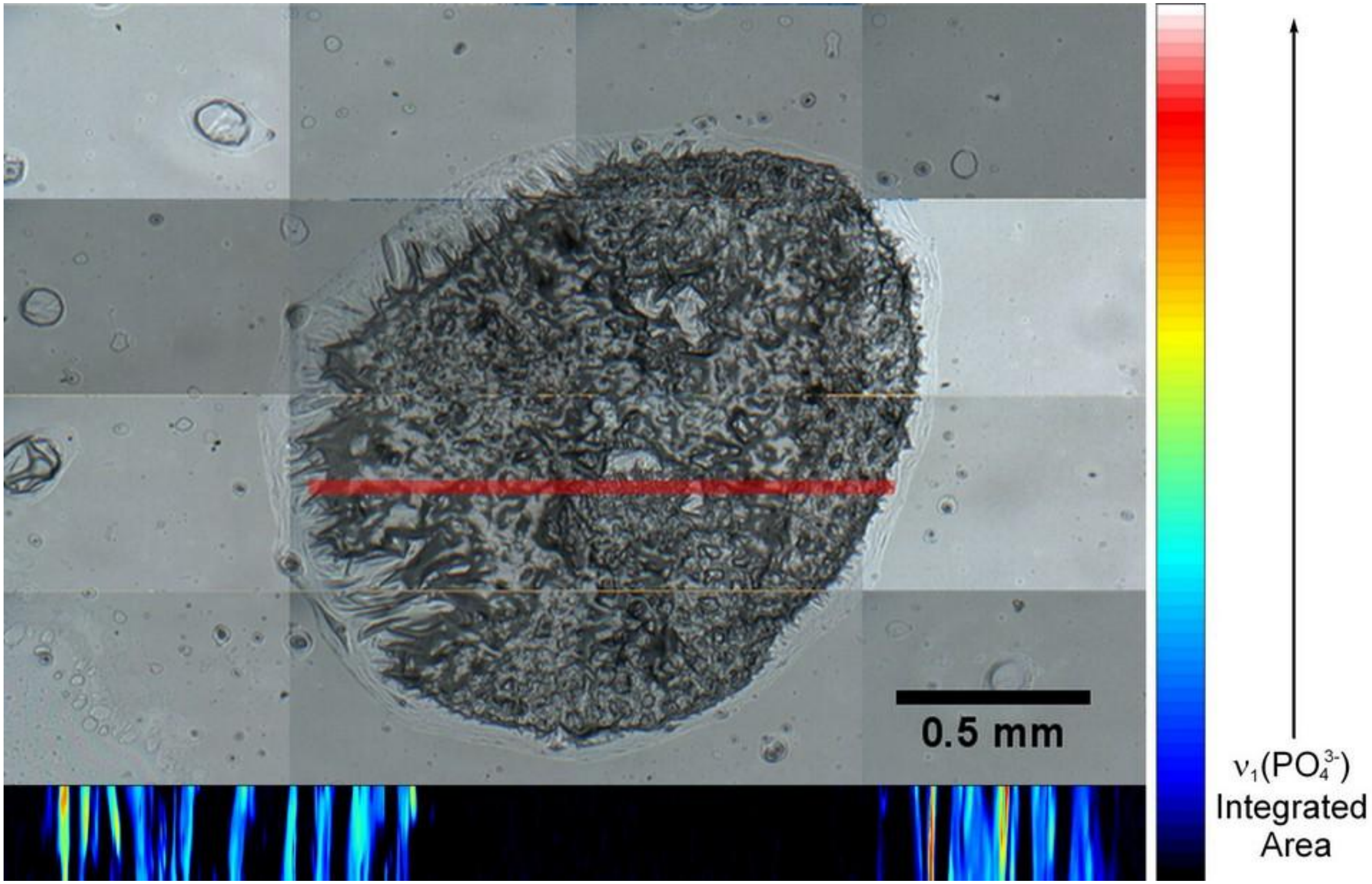

Figure 3.5: Top) Optical image of duplicate vehicle control tibiotarsus cross-section collected using the 10x objective of the confocal Raman microscope. The red inset (15 μm x 1500 μm) represents the area that was micro-Raman mapped. **Bottom)** Micro-Raman image of this area.[19]

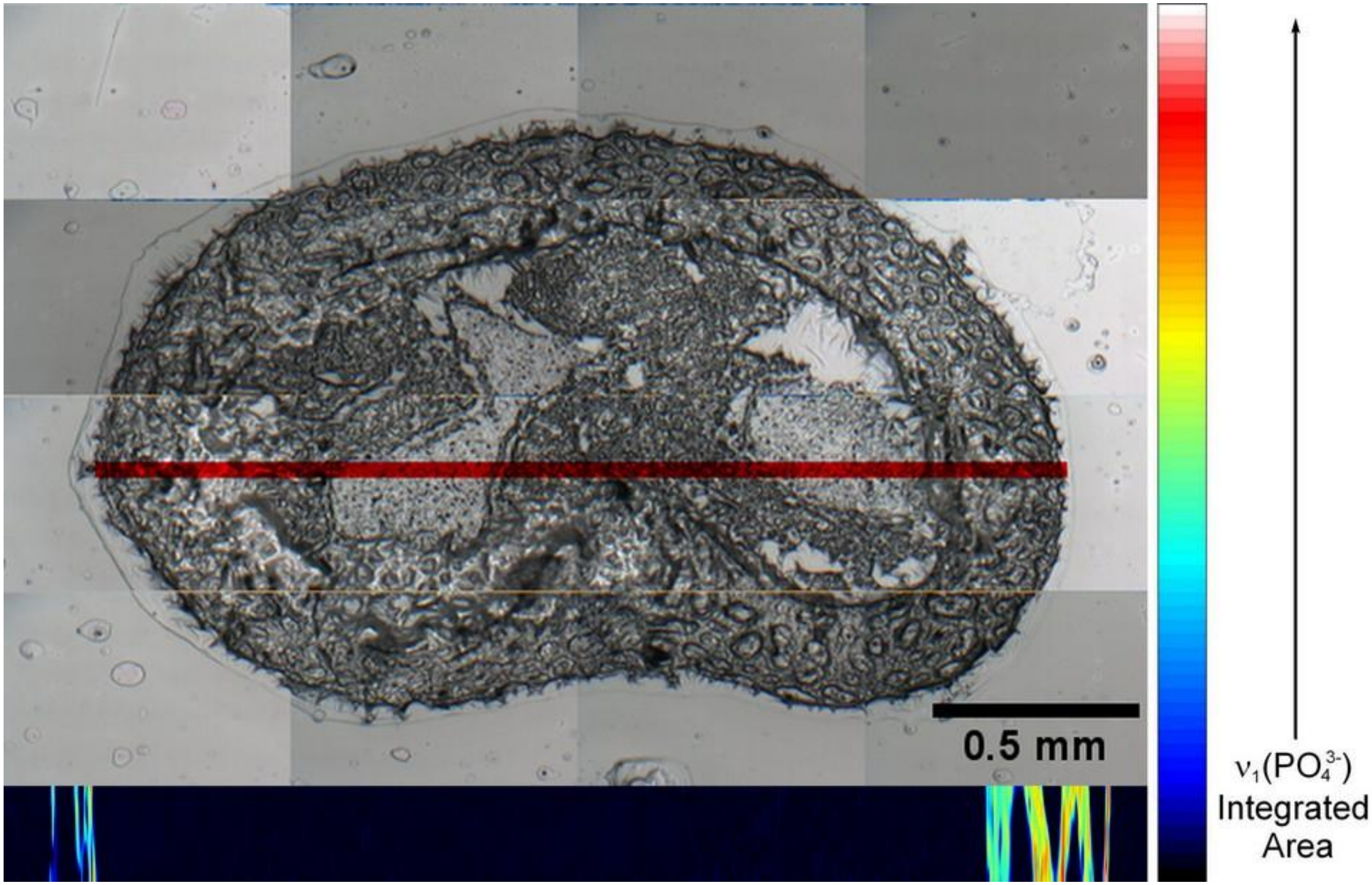

Figure 3.6: Top) Optical image of a Pd-treated tibiotarsus cross-section collected using the 10x objective of the confocal Raman microscope. The red inset (15 μm x 2332 μm) represents the area that was micro-Raman mapped. **Bottom)** Micro-Raman image of this area. [43]. (Micro-Raman map data collected by Monahan (2010)).[18, 19]

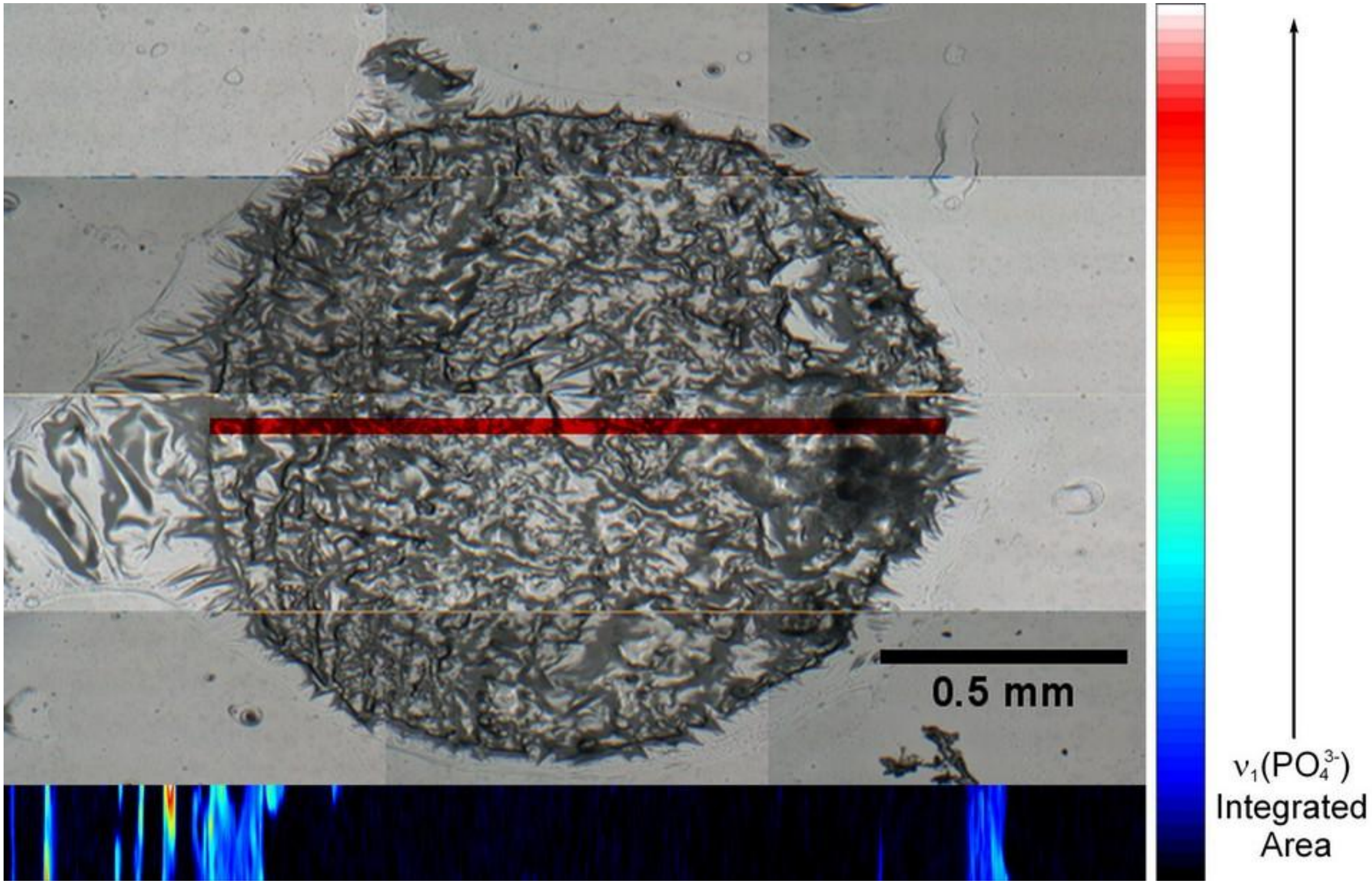

Figure 3.7: Top) Optical image of a second Pd-treated tibiotarsus cross-section collected using the 10x objective of the confocal Raman microscope. The red inset (15 μm x 1480 μm) represents the area that was micro-Raman mapped. **Bottom)** Micro-Raman image of this area.[19]

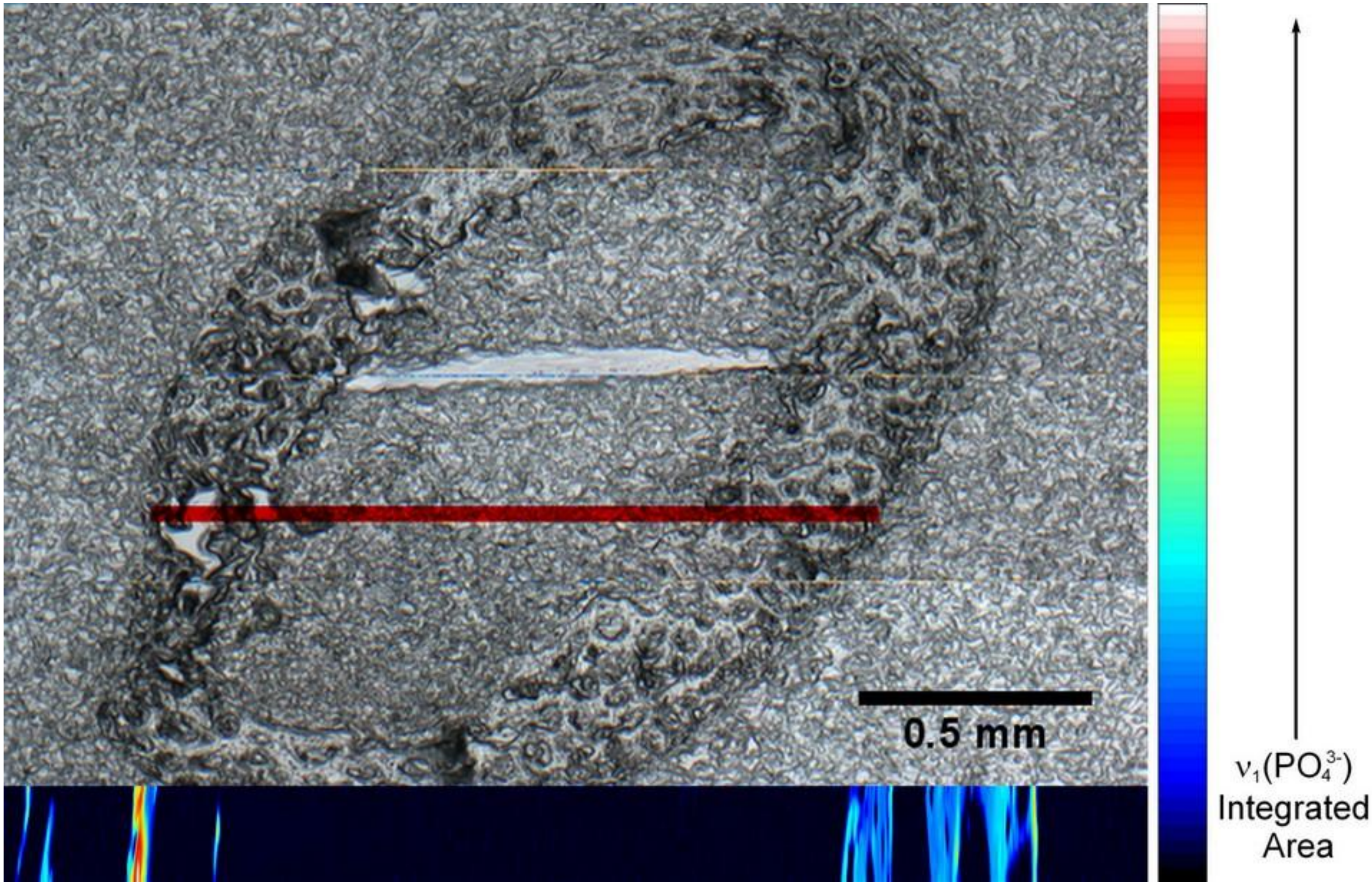

Figure 3.8: Top) Optical image of a Pt-treated tibiotarsus cross-section collected using the 10x objective of the confocal Raman microscope. The red inset (15 μm x 1557 μm) represents the area that was micro-Raman mapped. **Bottom)** Micro-Raman image of this area (Micro-Raman map data collected by Monahan (2010)).[18, 19]

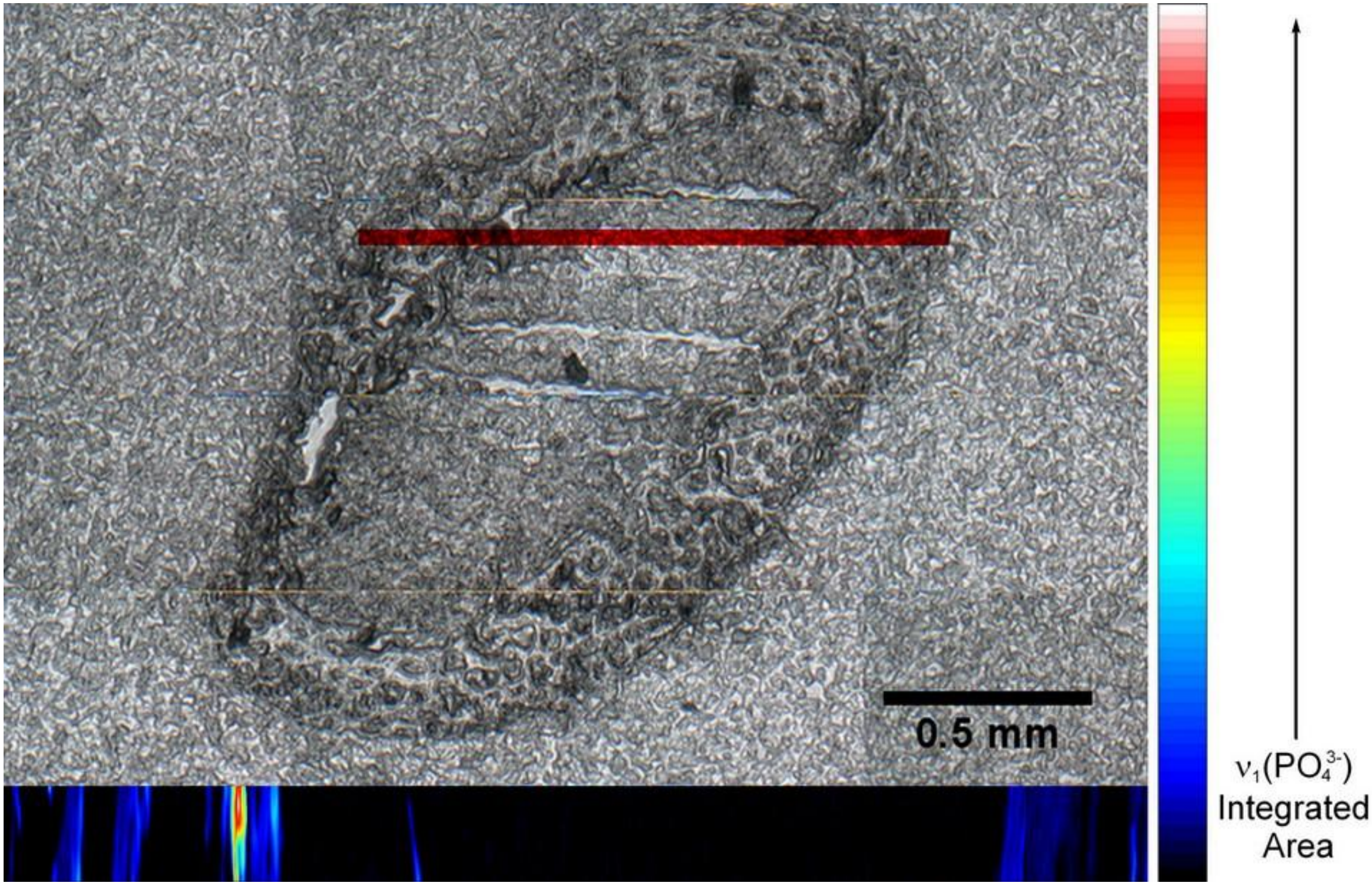

Figure 3.9: Top) Optical image of a Pt-treated tibiotarsus cross-section collected using the 10x objective of the confocal Raman microscope. The red inset (15 μm x 1411 μm) represents the area that was micro-Raman mapped. **Bottom)** Micro-Raman image of this area.[19]

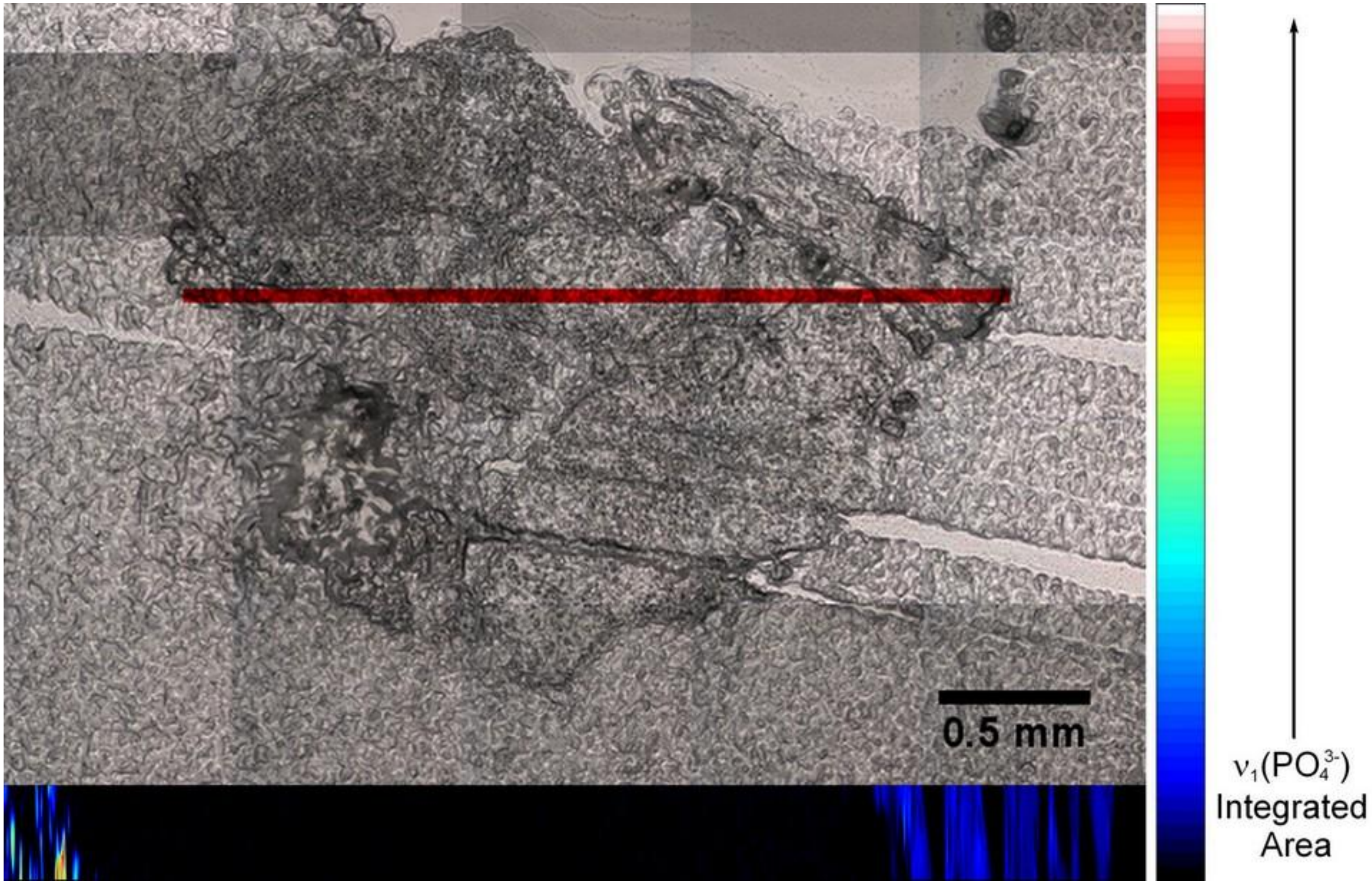

Figure 3.10 Top) Optical image of a Rh-treated tibiotarsus cross-section collected using the 10x objective of the confocal Raman microscope. The red inset (15 μm x 2690 μm) represents the area that was micro-Raman mapped. **Bottom)** Micro-Raman image of this area.[19]

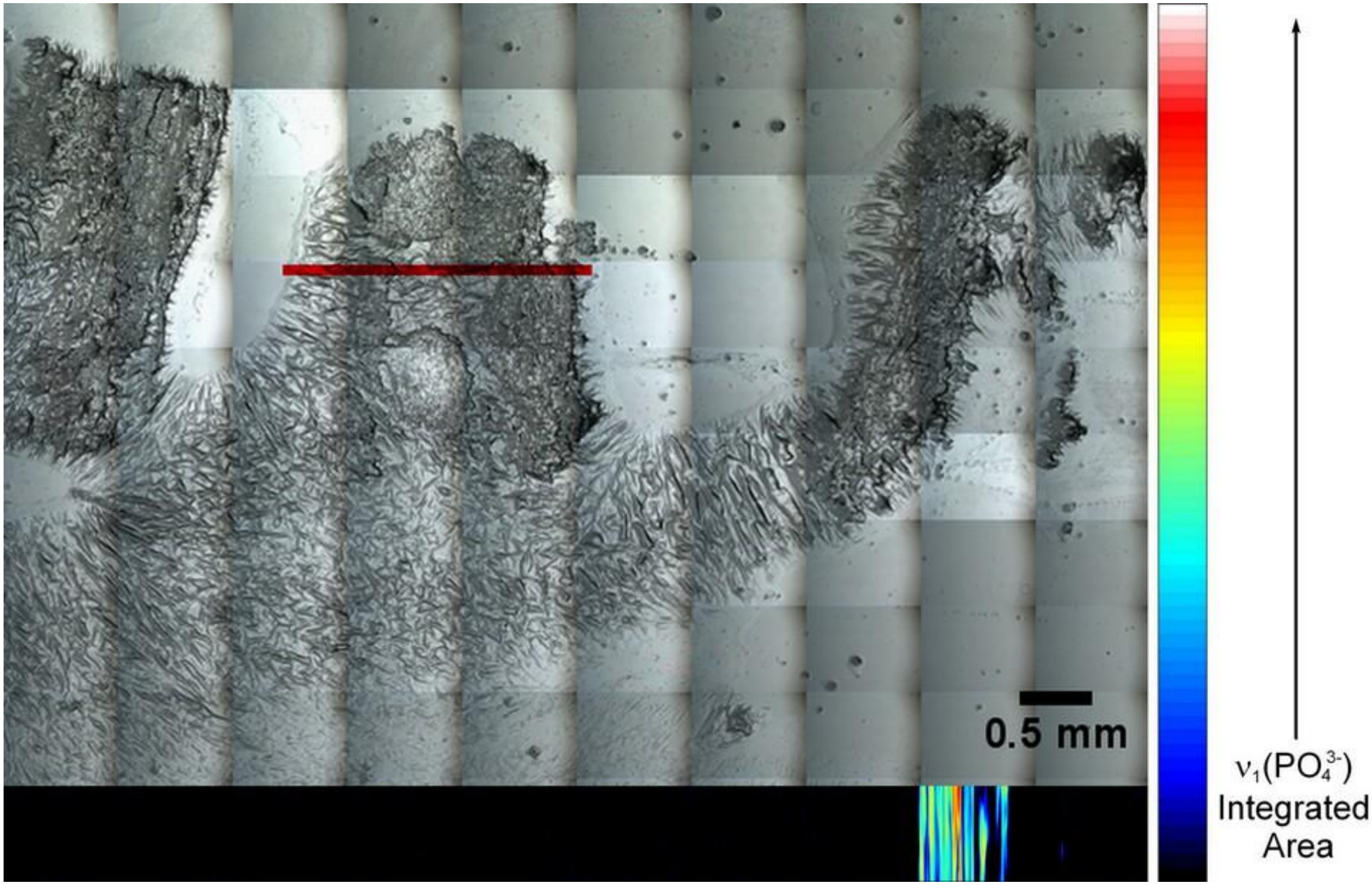

Figure 3.11: Top) Optical image of a duplicate Rh-treated tibiotarsus cross-section collected using the 10x objective of the confocal Raman microscope. The red inset (15 μm x 2100 μm) represents the area that was micro-Raman mapped. **Bottom)** Micro-Raman image of this area.[43] (Micro-Raman map data collected by Monahan (2010)).[18, 19]

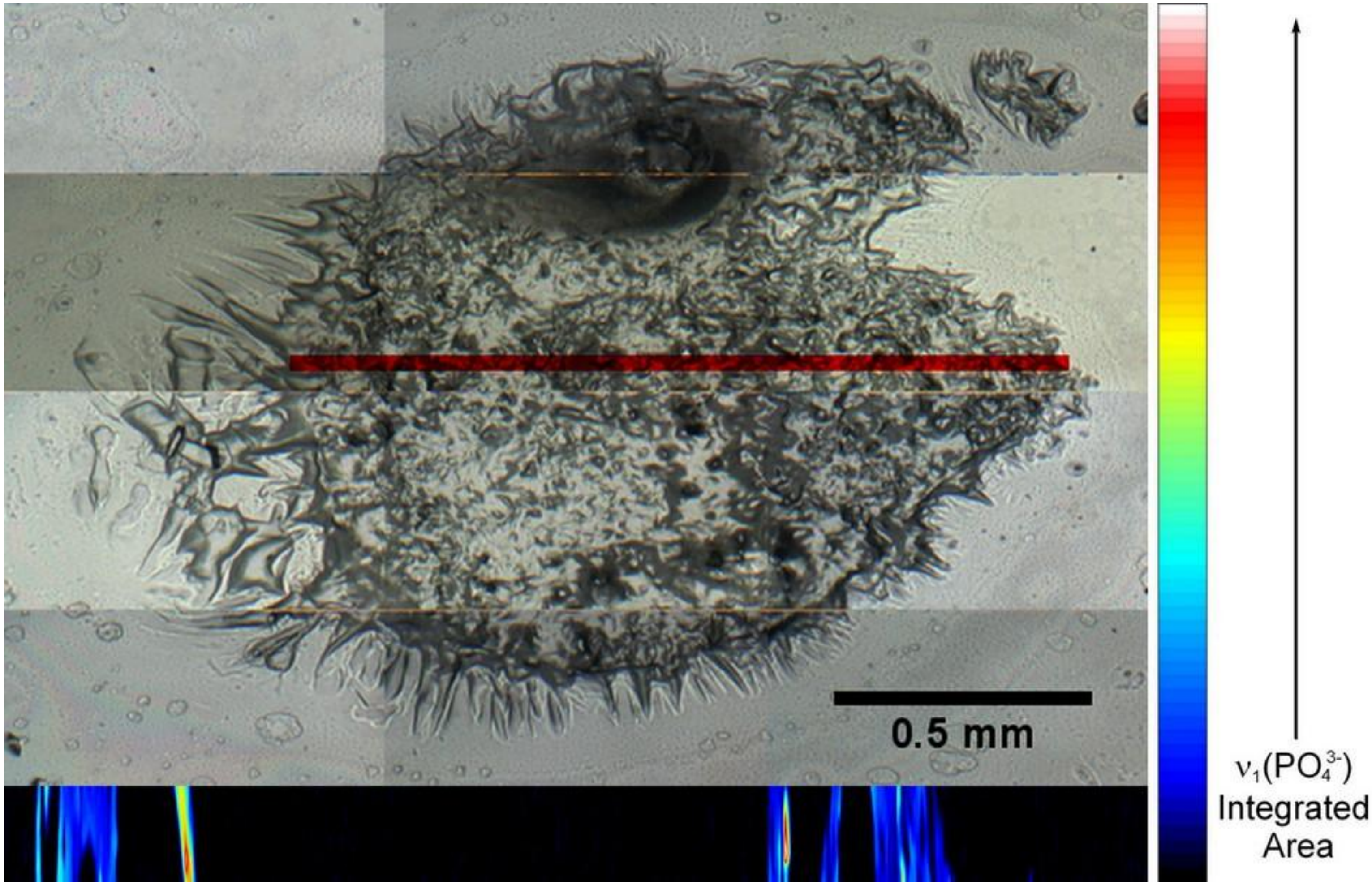

Figure 3.12: Top) Optical image of a PGM-mixture-treated tibiotarsus cross-section collected using the 10x objective of the confocal Raman microscope. The red inset (15 μm x 1500 μm) represents the area that was micro-Raman mapped. **Bottom)** Micro-Raman image of this area.[19]

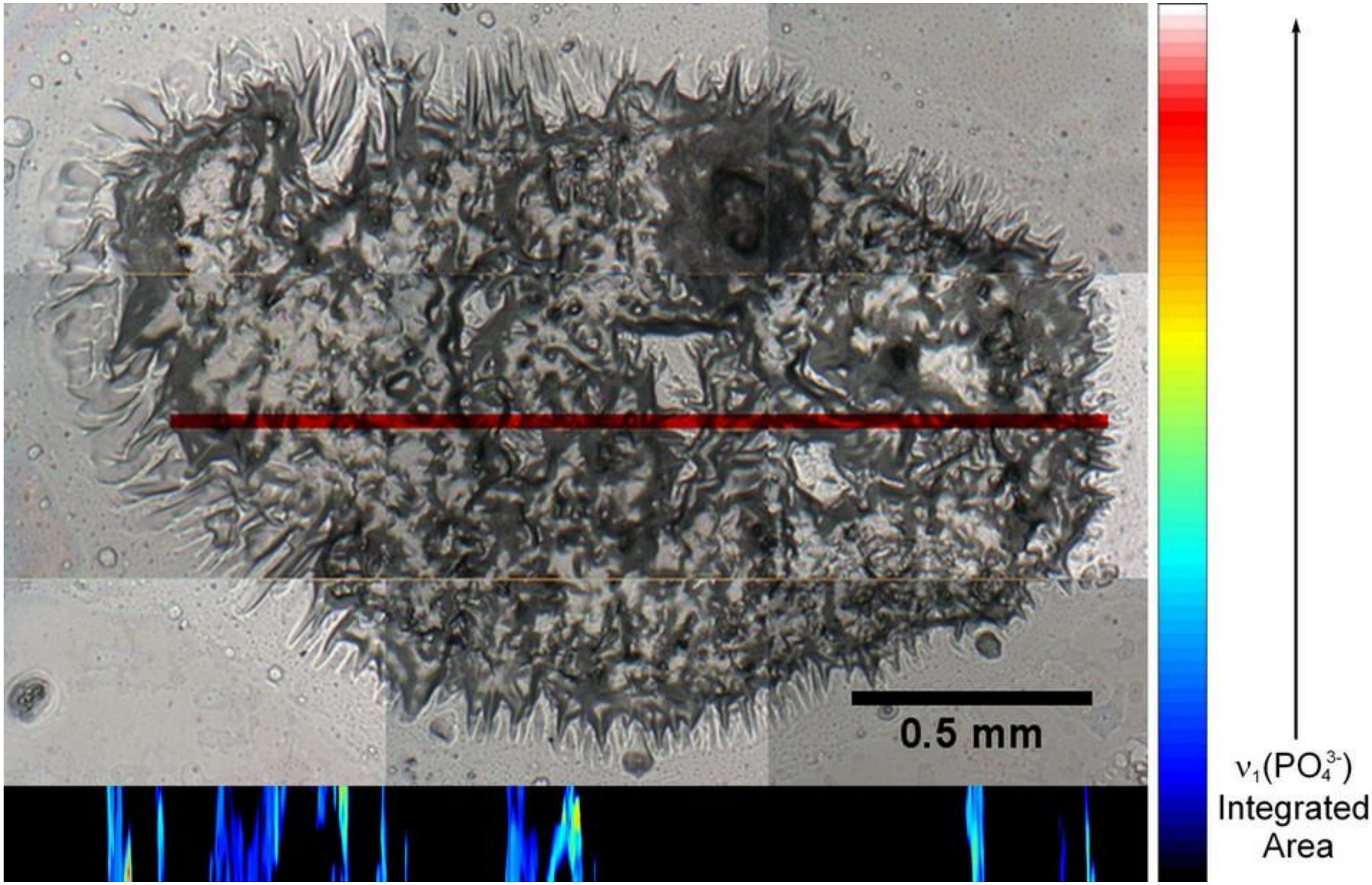

Figure 3.13: Top) Optical image of a second PGM-mixture-treated tibiotarsus cross-section collected using the 10x objective of the confocal Raman microscope. The red inset (15 μm x 1943 μm) represents the area that was micro-Raman mapped. **Bottom)** Micro-Raman image of this area (Micro-Raman map data collected by Monahan (2010)).[18, 19]

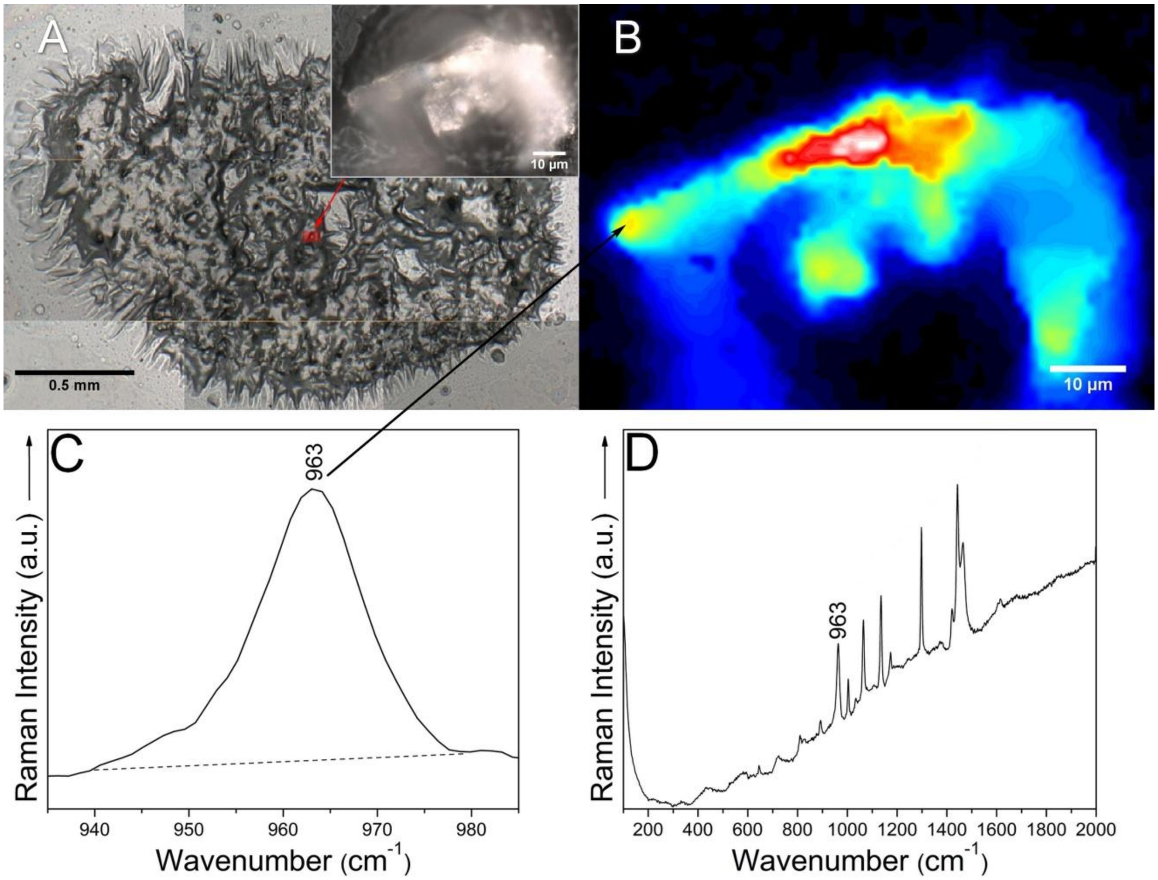

Figure 3.14: A) Optical image (10x objective) of a chick embryo tibiotarsus exposed to the PGM-mixture. **Inset:** Optical image (100x objective) of a highly mineralized region found within the medullary cavity indicated by red inset in panel A. **B)** Univariate micro-Raman image constructed from **C)** the baseline corrected integrated area of the phosphate band. **D)** A point Raman spectrum collected from the mineralized region between 100 cm^{-1} – 2000 cm^{-1}.[19]

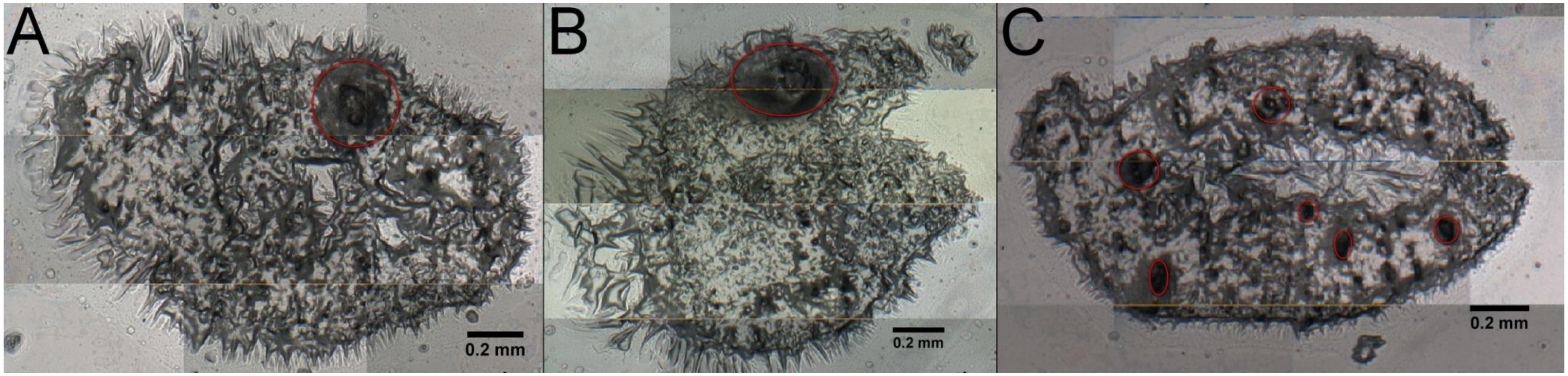

Figure 3.15: Optical images of PGM-mixture treated chick embryo tibiotarsus cross-sections (10x objective) from three specimens. Optical images **A)** and **B)** show the presence of large abnormal mineral inclusions. **C)** Tibiotarsus cross-section show several, smaller mineral inclusions. Point micro-Raman measurements confirmed the presence of anomalous mineral inclusions (denoted by red ellipses).[19]

3.3 Estimation of the age of mineral crystals of tibiotarsus cross-sections

The age of mineral crystals within the micro-Raman mapped areas of tibiotarsus cross-sections was estimated through the use of the custom written algorithm described in section 2.4. The tibiotarsi of chick embryos exposed to PGMs were found to have a statistically significant lower age of mineral crystals when compared to the control no injection (CNI) and the vehicle treatments (Kruskal-Wallis Anova on ranks ($p \leq 0.001$) and Dunn's multiple comparison tests ($p \leq 0.05$)).[19] Additionally, for specimens belonging to the same PGM-treatment group, the changes in the age of mineral crystals were not significantly different with the exception of the 1.0 ppm of Pd-treatment group (Figure 3.16).[19] However, this may be a result of the disparity in the sample size between the two specimens. For the Pd and Pt-treated embryos, the median age of mineral crystal values were approximately the same as the 75th percentile values of the controls. As in the observed mineral inclusions, these low ages of mineral crystals may be explained by an improperly developed periosteal bud. Osteogenic cells differentiate near capillaries of the periosteal bud. However, poor vascularization as a result of the anomalous calcium inclusions especially in the PGM-mixture group, could result in a delay of osteoblasts and osteoclasts differentiation.[27, 28]

It is expected that the age of mineral crystal values would vary considerably from pixel to pixel in cartilage tissue undergoing ossification. This was confirmed by the values estimated in MatLab and displayed in Figure 3.16. It can be seen that the age of mineral crystal values between the percentiles span a significantly smaller range in the treatment samples than for the controls. This is further evidence of a delay or disruption in the onset of ossification.[19] These abnormal age of mineral crystal values may be the result of an increase in the hydroxyapatite content that is initially secreted by the heterotrophic chondroblasts. This may also explain the presence of the mineral inclusions within the medullary cavity of the PGM mixture-treated tibiotarsi. Following ossification, the diaphysis is composed entirely of cancellous bone, which later is resorbed by osteoclasts in the inner regions of the diaphysis to form the marrow cavity. A disruption in the osteoclasts driven resorption process or increased amounts of initial hydroxyapatite may also explain the observed inclusions within the medullary cavity of the PGM-mixture treated tissue. [28, 29] However, whether the low age of mineral crystals values and a mineralized medullary cavity resulted from a delay in the onset of the ossification process or other unknown factors is currently still under investigation.[19]

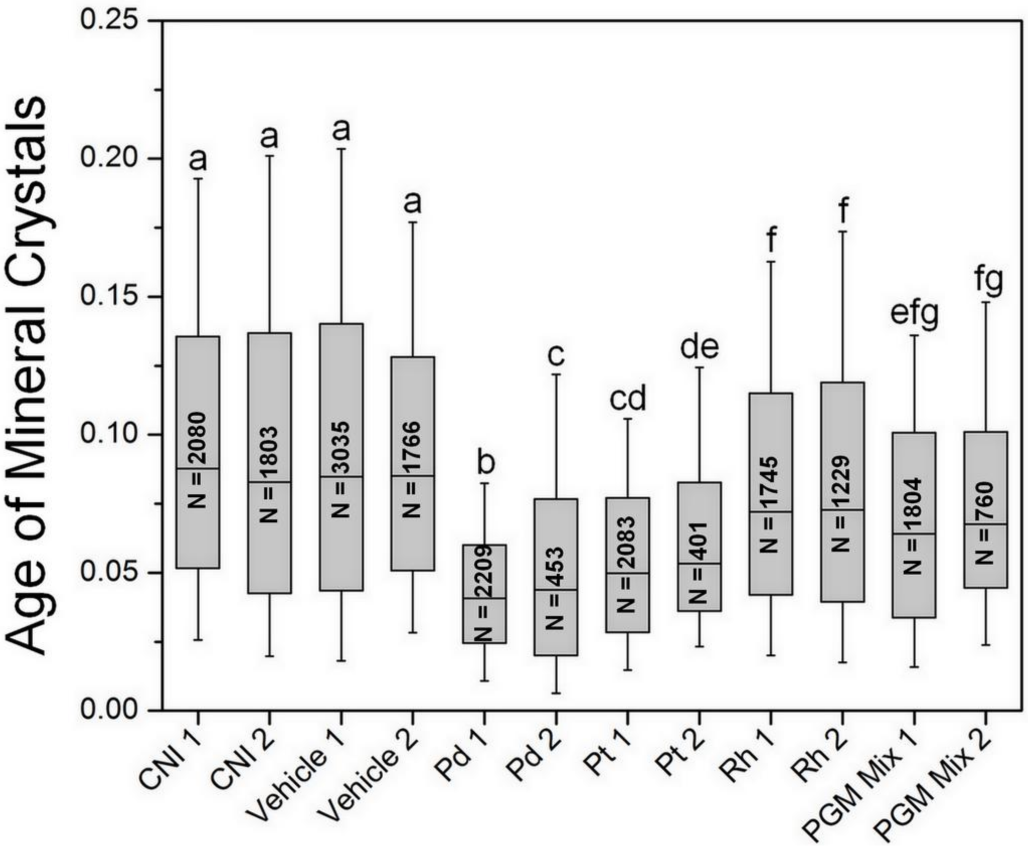

Figure 3.16: Quartile plot displaying the median value for the estimated age of mineral crystals. Center lines in grey boxes mark the median value. The 25th and 75th percentiles are represented by the top and bottom edges of shaded box, respectively. The whisker marks show the 10th and 90th percentiles (upper and lower marks, respectively). The number of pixels used to calculate the age of mineral crystals is denoted by *N* for each specimen. Statistical differences were detected by Kruskal-Wallis Anova on Ranks ($p \leq 0.001$) and determined by Dunn's multiple comparison tests ($p \leq 0.05$). Treatment or control values denoted with the same letter were not statistically different. [19]

4 CONCLUSIONS

In conclusion, micro-Raman spectroscopic imaging in conjunction with novel MatLab hyperspectral data processing confirmed the proposed hypothesis. Sublethal doses of 1.0 ppm of PGMs were found to negatively impact the ossification process in tibiotarsi of developing chick embryos. Morphological changes in tibiotarsus cross-sections included a conversion of cancellous (*i.e.*, spongy) bone to dense bone (for the Pd treatment), less dense perichondrial regions (for the Pt treatment), anomalous mineral inclusions (for the PGM-mixture treatment), and abnormally soft bone tissue (for the Rh treatment). The gross morphological changes that were observed in the optical images of the tibiotarsus cross-sections were supported by the micro-Raman results. A significant mineral redistribution was observed via micro-Raman imaging for the PGM-mixture treatment, which led to the formation of a large number of abnormal mineral inclusions within the perichondrium and including the medullary cavity. This may disrupt the long range diffusion of the cartilage tissue, and the vascularization process in both developing and mature bone tissue. Furthermore, the age of mineral crystals indicated a significantly younger bone tissue for the PGM-treated samples relative to the controls.

These abnormal mineral changes may explain the observed skeletal deformities and morphological changes. The results of this study raise major concerns about the increasing PGM levels in the environment and their health effects on humans. Because chick embryos are in the family of amniotes, similar conclusions may be extrapolated for pregnant women and their fetus. The possible oxidative damage-mediated mechanism(s) by which the PGMs induce the observed, abnormal calcium inclusions and the low value for the age of mineral crystals will be investigated in future studies.[19]

5 REFERENCES

1. Seiler, H.; Sigel, A.; Sigel, H. *Handbook on Metals in Clinical and Analytical Chemistry;* M. Decker: New York, 1994; p 753.
2. Unites States Environmental Protection Agency: http://www.epa.gov/oms/invntory/overview/solutions/milestones.htm#70 (accessed June, 2012).
3. International Platinum Group Metal Association, Catalytic Converters: Munich, Germany, International Platinum Group Metals Association: http://www.ipa-news.com/en/89-0-Catalytic+Converters.html (accessed June, 2012).
4. Diehl, D.; Gagnon, Z. *Water Air Soil Pollut.* **2007,** *184* (1-4), 255-267.
5. Hooda, P. S.; Miller, A.; Edwards, A. C. *Sci. Total Environ.* **2007,** *384 (1-3),* 384-392.
6. Alt, F.; Bambauer, A.; Hoppstock, K.; Mergler, B.; Toelg, G. *Fresenius' J. Anal. Chem.* **1993,** *346 (6-9),* 693-696.
7. Konig, H. P.; Hertel, R. F.; Kock, W.; Rosner, G. *Atmos. Environ.* **1992,** *26A (5),* 741-745.
8. Ely, J. C.; Neal, C. R.; Kulpa, C. F.; Schneegurt, M. A.; Seidler, J. A.; Jain, J. C. *Environ. Sci. Technol.* **2001,** *35 (19),* 3816-3822.

9. Zerini, F.; Wiseman, C.; Puttmann, W. *Environ. Sci. Techno.* **2007,** *41 (2),* 451-456.

10. Witeley, J. D. *Water Air Soil Pollut.* **2005,** *160* (1), 77-93.

11. Gagnon, Z. E.; Newkirk, C.; Hicks, S. *J. of Environ.l Sci. Heal. A* **2006,** *41*, 397-414.

12. Shahar, H.; Majid, A. *The Malaysian Journal of Analytical Sciences*. **2007,** *11* (1), 145-153.

13. Coroli, S.; Alimonti, A.; Petrucci, F.; Bocca, B.; Krachler, M.; Forastiere, F.; Scacerdote, M.; Mallone, S. *Spectrochimica Acta B* **2001,** *56,* 1241-1248.

14. Vaughan, G. T.; Florence, T. M. *Sci. Total Environ.* **1992,** *111 (1),* 47-58.

15. Farago, M. E.; Kavanagh, P.; Blanks, R.; Kelly, J.; Kazantzis, G.; Thornton, I.; Simpson, P.; Cook, J.; Delves, T.; Hall, G. *Analyst* **1998,** *123,* 451-454.

16. Casarett, L. J.; Doull, J. *Casarett and Doull's Toxicology: The Basic Science of Poisons,* 7th ed.; McGraw-Hill: New York; p 1310.

17. Gagnon, Z. E.; Patel, A. *Journal of Environmental Health and Science A* **2007,** *42 (3),* 381-387.

18. Monahan, J. L. Skeletal Pathology of Tibiotarsi in Chick Embryos to Platinum Group Metals by Micro-Raman Spectroscopy. M.S. Thesis, Wright State University, Dayton, OH, June 2010.

19. Stahler, A.C.; Monahan, J. L.; Dagher, J. M.; Baker, J. D.; Markopoulos, M.M.; Iragena, D. B.; NeJame, B. M.; Slaughter, R.; Felker, D.; Burrgraff, L. W.; Isaac, L. A. C.; Gagnon, Z. E.; Sizemore, I. E. P. Evaluating the abnormal ossification in tibiotarsi of developing chick embryos exposed to 1.0 ppm sublethal doses of platinum group metals by spectroscopic techniques. Bone, Submitted: June 2012

20. NIOSH pocket guide to chemical hazards available at http://www.cdc.gov/niosh/idlh/intridl4.html (accessed June, 2012).

21. Miljkovic M.; Chernenkp, T.; Romeo, M. J.; Bird, B.; Matthaus, C.; Diem, M. *Analyst* **2010**, *135*, 2002-2013.

22. National Institutes of Health Revitalization Act of 1993, Pub. L. 103-43, Sec. 205, (June 10, 1993).

23. Stern, C. *DEV. Cell.* **2005,** 8 (1), 9-17.

24. Cogburn, L. A.; Porter, T. E.; Duclos, M. J.; Simon, J.; Burgess, S. C.; Zhu, J. J.; Cheng, H. H.; Dodgson, J. B.; Burnside, J. *Poult. Sci.* **2007,** *86 (10)*, 2059-2094.

25. Wolpert, L. *Mech. Dev.* **2004,** *121 (9)*, 1015-1017.

26. Tickle, C. *Mech. Dev.* **2004,** *121 (9)*, 1019-1029.

27. Hamburger, V.; Hamilton, H. L. *J. Morphol.* **1951,** *88 (1)*, 49-92.

28. Bellairs, R.; Osmond, M. *The Atlas of Chick Embryo Development,* 2nd ed.; Academic Press: San Diego, 2005; p 470.

29. Cormack, D. H. *Essential Histology,* 2nd ed.; Lippincott Williams & Wilkins: Philadelphia, 2001; p 463.

30. Bronner, F.; Farach-Carson, M. C.; Roach, H. I., Ed. *Bone and Development*; Springer-Verlag London Limited: London 2010.

31. Proctor, N.; Lynch, P. *Manual of Ornithology: Avian Structure and Function;* Yale University Press: New Haven, 1998; p 342.

32. Garland, C. W.; Nibler, J. W.; Shoemaker, D. P. *Experiments in Physical Chemistry,* 8th ed.; McGraw-Hill: New York, 2009; p 734.

33. Silbey, R. J.; Alberty, R. A.; Bawendi, M. G. *Physical Chemistry,* 4th ed.; John Wiley & Sons, Inc: Hoboken, 2005; p 944.

34. Bernath, P. F. *Spectra of Atoms and Molecules;* Oxford University Press: New York, 1995; p 400.

35. LabSpec, version 5.45.09; DILOR; Lille, France, 2008.

36. MatLab, version 7.11.0.584 (R2010b); The Mathworks: Natick, MA, 2010.

37. Origin 8 SR4, version 8.0951(B951); OriginLab Corporation: Northampton, MA, 2008.

38. Akkus, O.; Polyakova-Akkus, A.; Adar, F.; Schaffler, M. B. *J. Bone Miner. Res.* **2003,** *18* (6), 10121019.

39. Kubisz, L.; Polomska, M. *Spectrochim. Acta A Mol. Biomol. Spectrosc.* **2007,** *66* (3), 616-625.

40. Penel, G.; Leroy, G.; Rey, C.; Bres, E. *Calcif. Tissue Int.* **1998,** *63,* 475-481.

41. Penl, G.; Delfosse, C.; Descamps, M.; Leroy, G. *Bone* **2005,** *36* (5), 893-901.

42. Van Apeldoorn, A. A.; Aksenov, Y.; Stigter, M. H. I.; de Bruijn, J. D.; Koerten, H. K.; Otto, C.; Greve, J.; van Blitterswijk, C. A. *J. R. Soc. Interface* **2005,** *2,* 39-45.

43. Faolain, E. O.; Hunter, M. B.; Byrne, J. M.; Kelehan, P.; Lamkin, H. A.; Byrne, H. J.; Lyng, F. M. *J. Histochem. Cytochem.* **2005,** *53* (1), 121-129.

44. SigmaPlot, version 11.0; Systat Software: San Jose, CA, 2010.

45. Abramoff, M.D.; Magalhaes, P.J.; Ram, S.J.; Biophotonics International **2004**, *11(7)*, 36-42.

46. Rosenburg, B. *Naturwiss.* **1973,** *60* (9), 399-406.

6 Addenda

Table A.1: Example of Micro-Raman map data as a text file (.txt). Spatial coordinates are in green, the wavenumber axis is the blue row vector, and the values in red are the Raman intensities for each pixel along the wavenumber axis.

Coordinates		Wavenumber (cm^{-1})									
Y	X	100	101.122	102.245	103.367	104.489	105.611	106.734	107.856	108.978	…
-7	-57	4444.42	4480.92	4470.81	4489.44	4451.44	4450.13	4370.04	4290.29	4209.33	…
-7	-56	4277.14	4343.49	4406.89	4428.94	4397.72	4326.55	4327.77	4242.02	4100.56	…
-7	-55	4251.52	4338.5	4355.12	4306.94	4276.52	4276.96	4195.07	4145.22	4051.97	…
-7	-54	4244.7	4312.99	4326.97	4344.65	4365.72	4207.66	4198.3	4145.09	4019.75	…
-7	-53	4326.19	4371.61	4399.26	4409.29	4353.72	4369.44	4283.95	4208.24	4154.98	…
-7	-52	4225.2	4276.73	4291.57	4375.82	4396.83	4273.7	4235.9	4183.35	4112.85	…
-7	-51	4319.87	4387.83	4433.46	4435.67	4424.32	4322.58	4269.17	4232.36	4163.78	…
-7	-50	4259.65	4322.71	4320.46	4297.12	4359.38	4280.79	4244.25	4195.15	4124.98	…
-7	-49	4292.83	4369.57	4398.74	4328.45	4394.96	4318.12	4322.32	4193.19	4115.05	…
-7	-48	4533.64	4561.28	4572.92	4571.94	4529.13	4477.61	4446.5	4349.53	4260.9	…
-7	-47	4659.92	4664.92	4601.56	4535.98	4566.8	4475.54	4339.67	4245.96	4153.62	…
-7	-46	4983.97	5017.71	4918.48	4768.13	4696.24	4592.75	4447.79	4347	4238.45	…
-7	-45	5136.22	5117.43	5084.03	5001.99	4886.24	4717.7	4580.08	4396.01	4221.79	…
-7	-44	5128.27	5088.77	5010.99	4892.57	4779.55	4661.23	4551.42	4392.03	4248.99	…
-7	-43	4905.13	4902.23	4906.47	4828.48	4728.48	4576.1	4455.44	4342.65	4214.04	…
-7	-42	5057.59	5029.36	4959.22	4880.75	4759.92	4671.28	4616.02	4478.8	4319.09	…
-7	-41	4756.42	4779.39	4746.92	4702.95	4641.85	4519.16	4445.55	4355.57	4218.34	…

6.1 Parsing micro-Raman map data

```
a.MS= x1ppm_HCl_Cont_Map_1; % Paste text file name in this line excluding extension

ACS.raw=a.MS(2:end,3:end); % Creates Spectral Data Block from Raman intensities

ACS.wn=a.MS(1,3:end); % extracts wave number axis
ACS.wn=ACS.wn';
ACS.wnMax=size(ACS.wn);
ACS.wnMax=max(ACS.wnMax); % Determines wavenumber maximum

ACS.dX=a.MS(2:end,2); % Creates spatial x dimensional variable
ACS.dX=unique(ACS.dX);
ACS.dX=size(ACS.dX);
ACS.dX=max(ACS.dX);

ACS.dY=a.MS(2:end,1); % Creates spatial y dimensional variable
ACS.dY=unique(ACS.dY);
ACS.dY=size(ACS.dY);
ACS.dY=max(ACS.dY);

ACS.Pixelnum=ACS.dY.*ACS.dX; % Number of pixels in the map

clear a % Removes redundant data

clear 'x1ppm_HCl_Cont_Map_1' % Paste text file name in this line excluding extension to remove redundant data.
```

6.2 Concatenating incremental micro-Raman map data

```
% Input dialogue box creation
a.prompt = {'Total Y-dimensions','Total X-dimensions', 'Concatenate: Vertically or Horizontally (V = 1, H = 2)'};
a.dlg_title = 'Stitcher';
a.num_lines = 1;
a.def = {'1','1','2'};
a.answer = inputdlg(a.prompt,a.dlg_title,a.num_lines,a.def);

% Input variable extraction
```

```
ACS.dX=a.answer(2,:);
ACS.dX=str2double(ACS.dX);
ACS.dY=a.answer(1,:);
ACS.dY=str2double(ACS.dY);
a.cat=a.answer(3,:);
a.cat=str2double(a.cat);

% Creates new map coordinates
ACS.Pixelnum= ACS.dX*ACS.dY;
ACS.wn=ACS1.wn;
ACS.wnMax=ACS1.wnMax;

% Reshapes individual Raman maps to proper orientation prior to concatenating
if exist ('ACS1')
m1=num2cell(ACS1.raw,2);
m1=reshape(m1,ACS1.dX,ACS1.dY)’;
end

if exist ('ACS2')
m2=num2cell(ACS2.raw,2);
m2=reshape(m2,ACS2.dX,ACS2.dY)’;
end

if exist ('ACS3')
m3=num2cell(ACS3.raw,2);
m3=reshape(m3,ACS3.dX,ACS3.dY);
end

if exist ('ACS4')
m4=num2cell(ACS4.raw,2);
m4=reshape(m4,ACS4.dX,ACS4.dY)’;
end

if exist ('ACS5')
m5=num2cell(ACS5.raw,2);
m5=reshape(m5,ACS5.dX,ACS5.dY)’;
end

if exist ('ACS6')
m6=num2cell(ACS6.raw,2);
m6=reshape(m6,ACS6.dX,ACS6.dY)’;
end

if exist ('ACS7')
m7=num2cell(ACS7.raw,2);
m7=reshape(m7,ACS7.dX,ACS7.dY)’;
```

```
end

if exist ('ACS8')
m8=num2cell(ACS8.raw,2);
m8=reshape(m8,ACS8.dX,ACS8.dY)’;
end

% Concatenates Raman maps
if exist ('ACS2');
Total_Map=cat(a.cat,m1,m2);
end

if exist ('ACS3');
Total_Map=cat(a.cat,m1,m2,m3);
end

if exist ('ACS4');
Total_Map=cat(a.cat,m1,m2,m3,m4);
end

if exist ('ACS5');
Total_Map=cat(a.cat,m1,m2,m3,m4,m5);
end

if exist ('ACS6');
Total_Map=cat(a.cat,m1,m2,m3,m4,m5,m6);
end

if exist ('ACS7');
Total_Map=cat(a.cat,m1,m2,m3,m4,m5,m6,m7);
end

if exist ('ACS8');
Total_Map=cat(a.cat,m1,m2,m3,m4,m5,m6,m7,m8);
end

% Reshapes datablock to proper spatial orientation
Whole_Map=reshape(Total_Map’,ACS.Pixelnum,[]);
ACS.raw=cell2mat(Whole_Map);
```

6.3 Univariate Image Construction

```
% Input dialogue box creation
a.prompt = {,'Image Type (A = Area, I = Intensity, D = Derivative)','Normalize
Spectra (No Normalization = N, Min/Max Normalization = MM, Unit Area
Normalization =A, or Standard Normal Variate =SNV)', 'Peak Ratio (Y = Yes. Y
= no)','Left 1 (cm-1):','Right 1 (cm-1):','Left 2 (cm-1):','Right 2 (cm-1):' 'Color
Map (jet, bone, ect.):','Filter Type (MF = Median Filter, LA = Linear Moving
Average, SG = Savitzky-Golay, NF = No Filter:)','Polynomial Order (For use in
Savitzky-Golay Filter or Derivative):',' Filter Window Size (Odd values <
FWHM):','Derivative Order','Image Median Spatial Filter (Y or N):', 'Interpolate
(Y or N):'};
a.dlg_title = 'Univariate Image';
a.num_lines = 1;
a.def =
{'A','MM','N','935','985','1050','1090','Custom','MF','2','11','2', 'N','Y'};
a.options.Resize='on';
a.options.WindowStyle='normal';
a.options.Interpreter='tex';
a.answer = inputdlg(a.prompt,a.dlg_title,a.num_lines,a.def,a.options);

% Input variable extraction
a.Type=a.answer(1,:);
a.Type=char(a.Type);
a.Norm=a.answer(2,:);
a.Norm=char(a.Norm);
a.ratio=a.answer(3,:);
a.ratio=char(a.ratio);
a.Color=a.answer(8,:);
a.Color=char(a.Color);
a.FT=a.answer(9,:);
a.FT=char(a.FT);
a.PO=a.answer(10,:);
a.PO=str2double(a.PO);
a.MW=a.answer(11,:);
a.MW=str2double(a.MW);
a.DO=a.answer(12,:);
a.DO=str2double(a.DO);
a.Median=a.answer(13,:);
a.Median=char(a.Median);
a.Inter=a.answer(14,:);
a.Inter=char(a.Inter);

a.Peak_1.left=a.answer(4,:);
a.Peak_1.right=a.answer(5,:);
```

```
a.Peak_1.left = char(a.Peak_1.left);
a.Peak_1.right = char(a.Peak_1.right);
a.Peak_1.left = str2double(a.Peak_1.left);
a.Peak_1.right = str2double(a.Peak_1.right);
a.Peak_1.leftx=find(ACS.wn>=a.Peak_1.left);
a.Peak_1.leftx=min(a.Peak_1.leftx);
a.Peak_1.rightx=find(ACS.wn<=a.Peak_1.right);
a.Peak_1.rightx=max(a.Peak_1.rightx);

a.Peak_2.left=a.answer(6,:);
a.Peak_2.right=a.answer(7,:);
a.Peak_2.left = char(a.Peak_2.left);
a.Peak_2.right = char(a.Peak_2.right);
a.Peak_2.left = str2double(a.Peak_2.left);
a.Peak_2.right = str2double(a.Peak_2.right);
a.Peak_2.leftx=find(ACS.wn>=a.Peak_2.left);
a.Peak_2.leftx=min(a.Peak_2.leftx);
a.Peak_2.rightx=find(ACS.wn<=a.Peak_2.right);
a.Peak_2.rightx=max(a.Peak_2.rightx);

 % Custom color map
if strcmpi(a.Color,'Custom')
  [a.Color] = Custom_CC;
end

% Recalls normalization functions
if strcmpi(a.Norm,'MM');
   [ACS.norm]=MMNorm(ACS.raw,ACS.wnMax);
end

if strcmpi(a.Norm,'A');
   [ACS.norm]=AreaNorm(ACS.raw,ACS.wnMax);
end

if strcmpi(a.Norm,'SNV');
   [ACS.norm]=SSNorm(ACS.raw);
end

% Recalls spectral smoothing functions and selects wavenumber integration limits
if strcmpi(a.FT,'NF');
a.Peak_1.Area1=ACS.raw(:,(a.Peak_1.leftx:a.Peak_1.rightx));
a.Peak_2.Area1=ACS.raw(:,(a.Peak_2.leftx:a.Peak_2.rightx));
end

if strcmpi(a.Norm,'N')==0;
a.Peak_1.Area1=ACS.norm(:,(a.Peak_1.leftx:a.Peak_1.rightx));
```

```
a.Peak_2.Area1=ACS.norm(:,(a.Peak_2.leftx:a.Peak_2.rightx));
end

if strcmpi(a.FT,'MF')&& strcmpi(a.Norm,'N');
a.a=size(ACS.wn);
a.a=a.a(:,1);
ACS.filt=medfilt1(ACS.raw,a.MW,a.a-1,2);
a.Peak_1.Area1=ACS.filt(:,(a.Peak_1.leftx:a.Peak_1.rightx));
a.Peak_2.Area1=ACS.filt(:,(a.Peak_2.leftx:a.Peak_2.rightx));
end

if strcmpi(a.FT,'LA')&& strcmpi(a.Norm,'N');
ACS.filt=filter(ones(1,a.MW)/a.MW,1,ACS.raw,[],2);
a.Peak_1.Area1=ACS.filt(:,(a.Peak_1.leftx:a.Peak_1.rightx));
a.Peak_2.Area1=ACS.filt(:,(a.Peak_2.leftx:a.Peak_2.rightx));
end

if strcmpi(a.FT,'SG')&& strcmpi(a.Norm,'N');
ACS.filt=sgolayfilt(ACS.raw,a.PO,a.MW,[],2);
a.Peak_1.Area1=ACS.filt(:,(a.Peak_1.leftx:a.Peak_1.rightx));
a.Peak_2.Area1=ACS.filt(:,(a.Peak_2.leftx:a.Peak_2.rightx));
end

if strcmpi(a.FT,'MF')&& strcmpi(a.Norm,'N')==0;
a.a=size(ACS.wn);
a.a=a.a(:,1);
ACS.filt=medfilt1(ACS.norm,a.MW,a.a-1,2);
a.Peak_1.Area1=ACS.filt(:,(a.Peak_1.leftx:a.Peak_1.rightx));
a.Peak_2.Area1=ACS.filt(:,(a.Peak_2.leftx:a.Peak_2.rightx));
end

if strcmpi(a.FT,'LA')&& strcmpi(a.Norm,'N')==0;
ACS.filt=filter(ones(1,a.MW)/a.MW,1,ACS.norm,[],2);
a.Peak_1.Area1=ACS.filt(:,(a.Peak_1.leftx:a.Peak_1.rightx));
a.Peak_2.Area1=ACS.filt(:,(a.Peak_2.leftx:a.Peak_2.rightx));
end

if strcmpi(a.FT,'SG')&& strcmpi(a.Norm,'N')==0;
ACS.filt=sgolayfilt(ACS.norm,a.PO,a.MW,[],2);
a.Peak_1.Area1=ACS.filt(:,(a.Peak_1.leftx:a.Peak_1.rightx));
a.Peak_2.Area1=ACS.filt(:,(a.Peak_2.leftx:a.Peak_2.rightx));
end

% Recalls Savitzky-Golay derivative functions
if strcmpi(a.Type, 'D') && strcmpi(a.Norm,'N')
   [a.D] = derivCoeff(ACS.raw,ACS.wnMax, a.MW, a.PO, a.DO);
```

```
   ACS.SGD=ACS.raw*a.D;
end

if strcmpi(a.Type, 'D') && strcmpi(a.Norm,'N')==0
[a.D] = derivCoeff(ACS.norm,ACS.wnMax, a.MW, a.PO, a.DO);
 ACS.SGD=ACS.norm*a.D;
end

if strcmpi(a.Type,'D')==1
a.dPeak_1.Area1=ACS.SGD(:,(a.Peak_1.leftx:a.Peak_1.rightx));
a.dPeak_1.Area2=sum(a.dPeak_1.Area1,2);
a.dPeak_1.Area3=mean(a.dPeak_1.Area2);
a.dPeak_1.Intensity=min(a.dPeak_1.Area1,[],2);
a.dPeak_1.newrightx=(a.Peak_1.rightx-a.Peak_1.leftx)+1;
a.dPeak_1.newleftx=1;
end

% Creation of local baseline and calculation of corrected peak area and intensity
of 1st peak
a.Peak_1.Area2=sum(a.Peak_1.Area1,2);
a.Peak_1.Area3=mean(a.Peak_1.Area2);
a.Peak_1.newrightx=(a.Peak_1.rightx-a.Peak_1.leftx)+1;
a.Peak_1.newleftx=1;

a.Peak_1.deltaY=a.Peak_1.Area1(:,a.Peak_1.newrightx)-
a.Peak_1.Area1(:,a.Peak_1.newleftx);
a.Peak_1.slope=a.Peak_1.deltaY/(a.Peak_1.newrightx-1);
a.Peak_1.Yint=a.Peak_1.Area1(:,1)-a.Peak_1.slope(:);
a.Peak_1.Yline=a.Peak_1.slope(:)*(a.Peak_1.newleftx:a.Peak_1.newrightx);
a.Peak_1.Yintc=repmat(a.Peak_1.Yint,1,a.Peak_1.newrightx);
a.Peak_1.YlineFin=a.Peak_1.Yline(:,(a.Peak_1.newleftx:a.Peak_1.newrightx))+a.
Peak_1.Yintc(:,(a.Peak_1.newleftx:a.Peak_1.newrightx));
a.Peak_1.baselinearea=a.Peak_1.Area1-a.Peak_1.YlineFin;
a.Peak_1.Intensity=max(a.Peak_1.baselinearea,[],2);
a.Peak_1.Intensity(a.Peak_1.Intensity==0)=1E-100;
a.Peak_1.IntensityC=repmat(a.Peak_1.Intensity,1,a.Peak_1.newrightx);
a.Peak_1.AverageIntensity=mean(a.Peak_1.Intensity);
a.Peak_1.MapMaxIntensity=max(a.Peak_1.Intensity);
a.Peak_1.baselinearea2=sum(a.Peak_1.baselinearea,2);
a.Peak_1.Areamax=max(a.Peak_1.baselinearea2);
a.Indexmax=find(a.Peak_1.Intensity==a.Peak_1.MapMaxIntensity);
a.Peak_1.baselinearea2(a.Peak_1.baselinearea2<0)=0;
a.Peak_1.baselineareaaverage=mean(a.Peak_1.baselinearea2);

if strcmpi(a.ratio, 'Y')==1
a.Peak_2.Area2=sum(a.Peak_2.Area1,2);
```

```
end

% Creation of local baseline and calculation of corrected peak area and intensity
of 2nd peak
a.Peak_2.Area3=mean(a.Peak_2.Area2);
a.Peak_2.newrightx=(a.Peak_2.rightx-a.Peak_2.leftx)+1;
a.Peak_2.newleftx=1;

a.Peak_2.deltaY=a.Peak_2.Area1(:,a.Peak_2.newrightx)-
a.Peak_2.Area1(:,a.Peak_2.newleftx);
a.Peak_2.slope=a.Peak_2.deltaY/(a.Peak_2.newrightx-1);
a.Peak_2.Yint=a.Peak_2.Area1(:,1)-a.Peak_2.slope(:);
a.Peak_2.Yline=a.Peak_2.slope(:)*(a.Peak_2.newleftx:a.Peak_2.newrightx);
a.Peak_2.Yintc=repmat(a.Peak_2.Yint,1,a.Peak_2.newrightx);
a.Peak_2.YlineFin=a.Peak_2.Yline(:,(a.Peak_2.newleftx:a.Peak_2.newrightx))+a.
Peak_2.Yintc(:,(a.Peak_2.newleftx:a.Peak_2.newrightx));
a.Peak_2.baselinearea=a.Peak_2.Area1-a.Peak_2.YlineFin;
a.Peak_2.Intensity=max(a.Peak_2.baselinearea,[],2);
a.Peak_2.Intensity(a.Peak_1.Intensity==0)=1E-100;
a.Peak_2.IntensityC=repmat(a.Peak_2.Intensity,1,a.Peak_2.newrightx);
a.Peak_2.AverageIntensity=mean(a.Peak_2.Intensity);
a.Peak_2.MapMaxIntensity=max(a.Peak_2.Intensity);
a.Peak_2.baselinearea2=sum(a.Peak_2.baselinearea,2);
a.Peak_2.Areamax=max(a.Peak_2.baselinearea2);
a.Indexmax=find(a.Peak_2.Intensity==a.Peak_2.MapMaxIntensity);
a.Peak_1.baselinearea2(a.Peak_2.baselinearea2<0)=0;
a.Peak_1.baselineareaaverage=mean(a.Peak_2.baselinearea2);
end

% Selects spectral value for image construction
if strcmpi(a.Type,'I')==1;
ACS.ChmImage=a.Peak_1.Intensity;
end

if strcmpi(a.Type,'A')==1
ACS.ChmImage=a.Peak_1.baselinearea2;
end

if strcmpi(a.Type,'D')==1
ACS.ChmImage=a.dPeak_1.Intensity*-1;
end

if strcmpi(a.ratio,'Y')==1 && strcmpi(a.Type,'I')==1;
ACS.ChmImage=a.Peak_1.Intensity./a.Peak_2.Intensity;
end
```

```
if strcmpi(a.ratio,'Y')==1 && strcmpi(a.Type,'A')==1;
ACS.ChmImage=a.Peak_1.baselinearea2./a.Peak_2.baselinearea2;
end

% Reshapes peak value to true orientation of the map
ACS.ChmImage=reshape(ACS.ChmImage,ACS.dX,ACS.dY)';

% Employs a spatial median filter upon the image
if strcmpi(a.Median,'Y')==1
ACS.ChmImage=medfilt2(ACS.ChmImage, 'symmetric');
end
if strcmpi(a.Median,'N')==1
ACS.ChmImage=ACS.ChmImage;
end

% Applies bicubic interpolation smoothing to the Raman image
if strcmpi(a.Inter,'Y')==1
ACS.ChmImage=imresize(ACS.ChmImage,32,'bicubic');
end

if strcmpi(a.Inter,'N')==1
ACS.ChmImage=ACS.ChmImage;
end

clear a
```

6.4 Creation of logical matrix

```
% Input dialogue box creation
a.prompt = {'1Left (cm-1):','1Right (cm-1):','Spectral Median Filter Window Size (Odd values < FWHM):','% of Maximum'};
a.dlg_title = 'All Phosphate';
a.num_lines = 1;
a.def = {'935','985','11','20'};
a.options.Resize='on';
a.options.WindowStyle='normal';
a.options.Interpreter='tex';
a.answer = inputdlg(a.prompt,a.dlg_title,a.num_lines,a.def,a.options);

% Input variable extraction
a.Peak_1.left = a.answer(1,:);
a.Peak_1.right = a.answer(2,:);
```

```
a.Peak_1.left = char(a.Peak_1.left);
a.Peak_1.right = char(a.Peak_1.right);
a.Peak_1.left = str2double(a.Peak_1.left);
a.Peak_1.right = str2double(a.Peak_1.right);
a.MW=a.answer(3,:);
a.MW=str2double(a.MW);
a.Percent_Max=a.answer(4,:);
a.Percent_Max=char(a.Percent_Max);
a.Percent_Max=str2double(a.Percent_Max);

% Custom color map
[ColMap] = Custom_CC

a.Peak_1.leftx=find(ACS.wn>=a.Peak_1.left);
a.Peak_1.leftx=min(a.Peak_1.leftx);
a.Peak_1.rightx=find(ACS.wn<=a.Peak_1.right);
a.Peak_1.rightx=max(a.Peak_1.rightx);

a.Peak_1.leftx=find(ACS.wn>=a.Peak_1.left);
a.Peak_1.leftx=min(a.Peak_1.leftx);
a.Peak_1.rightx=find(ACS.wn<=a.Peak_1.right);
a.Peak_1.rightx=max(a.Peak_1.rightx);

% Application of median spectral filter
a.Filtered=medfilt1(ACS.raw,a.MW,1693,2);
a.Peak_1.Area1=a.Filtered(:,(a.Peak_1.leftx:a.Peak_1.rightx));

% Selects wavenumber integration limits
a.Peak_1.Area2=sum(a.Peak_1.Area1,2);
a.Peak_1.Area3=mean(a.Peak_1.Area2);
a.Peak_1.newrightx=(a.Peak_1.rightx-a.Peak_1.leftx)+1;
a.Peak_1.newleftx=1;

% Creation of local baseline and calculation of corrected peak area and intensity of peak
a.Peak_1.deltaY=a.Peak_1.Area1(:,a.Peak_1.newrightx)-a.Peak_1.Area1(:,a.Peak_1.newleftx);
a.Peak_1.slope=a.Peak_1.deltaY/(a.Peak_1.newrightx-1);
a.Peak_1.Yint=a.Peak_1.Area1(:,1)-a.Peak_1.slope(:);
a.Peak_1.Yline=a.Peak_1.slope(:)*(a.Peak_1.newleftx:a.Peak_1.newrightx);
a.Peak_1.Yintc=repmat(a.Peak_1.Yint,1,a.Peak_1.newrightx);
a.Peak_1.YlineFin=a.Peak_1.Yline(:,(a.Peak_1.newleftx:a.Peak_1.newrightx))+a.Peak_1.Yintc(:,(a.Peak_1.newleftx:a.Peak_1.newrightx));
a.Peak_1.baselinearea=a.Peak_1.Area1-a.Peak_1.YlineFin;
a.Peak_1.baselinearea(a.Peak_1.baselinearea<0)=0;
a.Peak_1.Intensity=max(a.Peak_1.baselinearea,[],2);
```

```
a.Peak_1.MapMaxIntensity=max(a.Peak_1.Intensity);
a.Peak_1.IntensityC=repmat(a.Peak_1.Intensity,1,a.Peak_1.newrightx);
a.Peak_1.AverageIntensity=mean(a.Peak_1.Intensity);
a.Peak_1.baselinearea2=sum(a.Peak_1.baselinearea,2);
a.Peak_1.Areamax=max(a.Peak_1.baselinearea2);
a.Peak_1.baselinearea2(a.Peak_1.baselinearea2<0)=0;
a.Peak_1.baselineareaaverage=mean(a.Peak_1.baselinearea2);

a.Chemical_Image=a.Peak_1.Intensity;
a.Chemical_Image=reshape(a.Chemical_Image,ACS.dX,ACS.dY)’;

% Creates logical matrix to be indexed against raw micro-Raman map
a.Chemical_Image1=a.Peak_1.Intensity;
 a.Chemical_Image1=reshape(a.Chemical_Image1,ACS.dX,ACS.dY)’;
a.Chemical_Image1(a.Chemical_Image1
<a.Percent_Max*0.01*a.Peak_1.MapMaxIntensity)=0;
a.Chemical_Image1(a.Chemical_Image1
>a.Percent_Max*0.01*a.Peak_1.MapMaxIntensity)=1;

a.Map_Image1= a.Chemical_Image1)’;
a.Map_Image1=reshape(a.Map_Image1,ACS.Pixelnum,1);
a.Map_Image1=repmat(a.Map_Image1,1,ACS.wnMax);

a.A=(a.Map_Image1.*ACS.raw);
a.B=a.A;
a.B(a.B==0)=[];
a.C=size(a.B);
a.C=max(a.C);
a.C=a.C/ACS.wnMax;

% Creates row vectors of spectra with signal intensity above selected threshold
ACS.ROIraw=reshape(a.B,a.C,ACS.wnMax);
```

6.5 Age of mineral crystals calculation

```
% Input dialogue box creation
a.prompt = {'1Left (cm-1):','1Right (cm-1):', '2Left (cm-1):','2Right (cm-1):','3Left
(cm-1):','3Right (cm-1):'};
a.dlg_title = 'AOM Calculation';
a.num_lines = 1;
a.def = {'930','986','1050','1090','1283','1317'};
a.options.Resize='on';
```

```
a.options.WindowStyle='normal';
a.options.Interpreter='tex';
a.answer = inputdlg(a.prompt,a.dlg_title,a.num_lines,a.def,a.options);

 % Input variable extraction
a.Peak_1.left = a.answer(1,:);
a.Peak_1.right = a.answer(2,:);
a.Peak_1.left = char(a.Peak_1.left);
a.Peak_1.right = char(a.Peak_1.right);
a.Peak_1.left = str2double(a.Peak_1.left);
a.Peak_1.right = str2double(a.Peak_1.right);
a.Peak_2.left = a.answer(3,:);
a.Peak_2.right = a.answer(4,:);
a.Peak_2.left = char(a.Peak_2.left);
a.Peak_2.right = char(a.Peak_2.right);
a.Peak_2.left = str2double(a.Peak_2.left);
a.Peak_2.right = str2double(a.Peak_2.right);
a.Peak_3.left = a.answer(5,:);
a.Peak_3.right = a.answer(6,:);
a.Peak_3.left = char(a.Peak_3.left);
a.Peak_3.right = char(a.Peak_3.right);
a.Peak_3.left = str2double(a.Peak_3.left);
a.Peak_3.right = str2double(a.Peak_3.right);

% Selects wavenumber integration limits
a.Peak_1.leftx=find(ACS.wn>=a.Peak_1.left);
a.Peak_1.leftx=min(a.Peak_1.leftx);
a.Peak_1.rightx=find(ACS.wn<=a.Peak_1.right);
a.Peak_1.rightx=max(a.Peak_1.rightx);
a.Peak_2.leftx=find(ACS.wn>=a.Peak_2.left);
a.Peak_2.leftx=min(a.Peak_2.leftx);
a.Peak_2.rightx=find(ACS.wn<=a.Peak_2.right);
a.Peak_2.rightx=max(a.Peak_2.rightx);
a.Peak_3.leftx=find(ACS.wn>=a.Peak_3.left);
a.Peak_3.leftx=min(a.Peak_3.leftx);
a.Peak_3.rightx=find(ACS.wn<=a.Peak_3.right);
a.Peak_3.rightx=max(a.Peak_3.rightx);

% Plots average spectrum
a.AverageSpectrum=mean(ACS.ROIraw,1);
a.AverageSpectrum_wn=rot90(a.AverageSpectrum,3);
a.Pixel_Spectrum_min=min(a.AverageSpectrum);
a.Pixel_Spectrum_max=max(a.AverageSpectrum);
line(ACS.wn,a.AverageSpectrum,'color', [0 0 0]);
title('Average Pixel Spectrum')
```

```
axis ([ACS.wn(1,1) ACS.wn(ACS.wnMax,1) a.Pixel_Spectrum_min
a.Pixel_Spectrum_max]);
box on
xlabel('Wavenumber (cm-1)')
ylabel('Raman Intensity (au)')

% Creation of local baseline and calculation of corrected peak area and intensity
of 1st peak
a.Peak_1.Area1=ACS.ROIraw(:,(a.Peak_1.leftx:a.Peak_1.rightx));
a.Peak_1.Area2=sum(a.Peak_1.Area1,2);
a.Peak_1.Area3=mean(a.Peak_1.Area2);
a.Peak_1.newrightx=(a.Peak_1.rightx-a.Peak_1.leftx)+1;
a.Peak_1.newleftx=1;

a.Peak_1.deltaY=a.Peak_1.Area1(:,a.Peak_1.newrightx)-
a.Peak_1.Area1(:,a.Peak_1.newleftx);
a.Peak_1.slope=a.Peak_1.deltaY/(a.Peak_1.newrightx-1);
a.Peak_1.Yint=a.Peak_1.Area1(:,1)-a.Peak_1.slope(:);
a.Peak_1.Yline=a.Peak_1.slope(:)*(a.Peak_1.newleftx:a.Peak_1.newrightx);
a.Peak_1.Yintc=repmat(a.Peak_1.Yint,1,a.Peak_1.newrightx);
a.Peak_1.YlineFin=a.Peak_1.Yline(:,(a.Peak_1.newleftx:a.Peak_1.newrightx))+a.
Peak_1.Yintc(:,(a.Peak_1.newleftx:a.Peak_1.newrightx));
a.Peak_1.baselinearea=a.Peak_1.Area1-a.Peak_1.YlineFin;
a.Peak_1.Intensity=max(a.Peak_1.baselinearea,[],2);
a.Peak_1.IntensityC=repmat(a.Peak_1.Intensity,1,a.Peak_1.newrightx);
a.Peak_1.averageIntensity=mean(a.Peak_1.Intensity);a.Peak_1.baselinearea(a.Pea
k_1.baselinearea<0)=0;
a.Peak_1.baselinearea2=sum(a.Peak_1.baselinearea,2);
a.Peak_1.baselinearea2(a.Peak_1.baselinearea2<0)=[];
a.Peak_1.Areamax=max(a.Peak_1.baselinearea2);
a.Peak_1.baselinearea2(a.Peak_1.baselinearea2<0)=0;
a.Peak_1.baselineareaaverage=mean(a.Peak_1.baselinearea2);

% Creation of local baseline and calculation of corrected peak area and intensity
of 2nd peak
a.Peak_2.Area1=ACS.ROIraw(:,(a.Peak_2.leftx:a.Peak_2.rightx));
a.Peak_2.Area2=sum(a.Peak_2.Area1,2);
a.Peak_2.Area3=mean(a.Peak_2.Area2);
a.Peak_2.newrightx=(a.Peak_2.rightx-a.Peak_2.leftx)+1;
a.Peak_2.newleftx=1;

a.Peak_2.deltaY=a.Peak_2.Area1(:,a.Peak_2.newrightx)-
a.Peak_2.Area1(:,a.Peak_2.newleftx);
a.Peak_2.slope=a.Peak_2.deltaY/(a.Peak_2.newrightx-1);
a.Peak_2.Yint=a.Peak_2.Area1(:,1)-a.Peak_2.slope(:);
a.Peak_2.Yline=a.Peak_2.slope(:)*(a.Peak_2.newleftx:a.Peak_2.newrightx);
```

```
a.Peak_2.Yintc=repmat(a.Peak_2.Yint,1,a.Peak_2.newrightx);
a.Peak_2.YlineFin=a.Peak_2.Yline(:,(a.Peak_2.newleftx:a.Peak_2.newrightx))+a.Peak_2.Yintc(:,(a.Peak_2.newleftx:a.Peak_2.newrightx));
a.Peak_2.baselinearea=a.Peak_2.Area1-a.Peak_2.YlineFin;
a.Peak_2.Intensity=max(a.Peak_2.baselinearea,[],2);
a.Peak_2.IntensityC=repmat(a.Peak_2.Intensity,1,a.Peak_2.newrightx);
a.Peak_2.averageIntensity=mean(a.Peak_2.Intensity);
a.Peak_2.baselinearea2=sum(a.Peak_2.baselinearea,2);
a.Peak_2.Areamax=max(a.Peak_2.baselinearea2);
a.Peak_2.baselinearea2(a.Peak_2.baselinearea2<0)=0;
a.Peak_2.baselineareaaverage=mean(a.Peak_2.baselinearea2);

% Creation of local baseline and calculation of corrected peak area and intensity of 3rd peak
a.Peak_3.Area1=ACS.ROIraw(:,(a.Peak_3.leftx:a.Peak_3.rightx));
a.Peak_3.Area2=sum(a.Peak_3.Area1,2);
a.Peak_3.Area3=mean(a.Peak_3.Area2);
a.Peak_3.newrightx=(a.Peak_3.rightx-a.Peak_3.leftx)+1;
a.Peak_3.newleftx=1;

a.Peak_3.deltaY=a.Peak_3.Area1(:,a.Peak_3.newrightx)-a.Peak_3.Area1(:,a.Peak_3.newleftx);
a.Peak_3.slope=a.Peak_3.deltaY/(a.Peak_3.newrightx-1);
a.Peak_3.Yint=a.Peak_3.Area1(:,1)-a.Peak_3.slope(:);
a.Peak_3.Yline=a.Peak_3.slope(:)*(a.Peak_3.newleftx:a.Peak_3.newrightx);
a.Peak_3.Yintc=repmat(a.Peak_3.Yint,1,a.Peak_3.newrightx);
a.Peak_3.YlineFin=a.Peak_3.Yline(:,(a.Peak_3.newleftx:a.Peak_3.newrightx))+a.Peak_3.Yintc(:,(a.Peak_3.newleftx:a.Peak_3.newrightx));
a.Peak_3.baselinearea=a.Peak_3.Area1-a.Peak_3.YlineFin;
a.Peak_3.Intensity=max(a.Peak_3.baselinearea,[],2);
a.Peak_3.IntensityC=repmat(a.Peak_3.Intensity,1,a.Peak_3.newrightx);
a.Peak_3.averageIntensity=mean(a.Peak_3.Intensity);
a.Peak_3.baselinearea2=sum(a.Peak_3.baselinearea,2);
a.Peak_3.Areamax=max(a.Peak_3.baselinearea2);
a.Peak_3.baselinearea2(a.Peak_3.baselinearea2<0)=0;
a.Peak_3.baselineareaaverage=mean(a.Peak_3.baselinearea2);

a.Peak_3.baselinearea2Avec=(a.Peak_3.baselinearea2.*0.698618258);

% Calculates age of mineral crystals
AOMInfo.aveCorrected1070Area=(a.Peak_2.baselinearea2-a.Peak_3.baselinearea2Avec);
AOMInfo.AOMAve=(AOMInfo.aveCorrected1070Area./a.Peak_1.baselinearea2;
AOMInfo.AOMAvenew=AOMInfo.AOMAve;
AOMInfo.AOMAvenew(AOMInfo.AOMAvenew<0)=[];
AOMInfo.AOMAvenew(AOMInfo.AOMAvenew<0)=[];
```

```
AOMInfo.AOMAvenew(AOMInfo.AOMAvenew==inf)=[];
AOMInfo.AverageAOMAvenew=nanmean(AOMInfo.AOMAvenew)
AOMInfo.AveSDofAOM=nanstd(AOMInfo.AOMAvenew)
```

7 Curriculum Vitae

ADAM CHRISTOPHER STAHLER
1024 Columbia Ave., Fairborn, OH. 45324 | (937) 407-0208 | stahler.5@wright.edu

EDUCATION

M.S., Chemistry, Wright State University **June 2010-Present**
Advisor: Dr. Ioana Pavel Sizemore

- Current GPA: 4.00
- Anticipated Graduation Date: **August 2012**

B.S., Biological Science Chemistry Dual, Wright State University **June 2010**

- *GPA: 3.939*
- *sum cum laude*

HONORS AND AWARDS

- Outstanding Graduate Teaching Assistant, WSU **June 2011/2012**
- Wright State University's Graduate Council Fellowship Award **March 2012**
- Wright State University's Chemistry Department

  Graduate Student Excellence Award **May 2012**

PUBLICATIONS

- Ioana E. Pavel, Khadijeh S. Alnajjar, Jennifer L. Monahan, Adam Stahler, Nora E. Hunter, Kent M. Weaver, Joshua D. Baker, Allie J. Meyerhoefer, and David A. Dolson. Estimating the Analytical and Surface Enhancement Factors in Surface-Enhanced Raman Scattering (SERS): A Novel Physical Chemistry and Nanotechnology Laboratory Experiment. *Journal of Chemical Education*, 2012, 89 (2), pp 286-290.

- Catherine B. Anders, Joshua D. Baker, Adam C. Stahler, Austin J. Williams, Dawn P. Wooley and Ioana E. Pavel Sizemore. Tangential Flow Ultrafiltration: A "Green" Method for the Size Selection and Concentration of Colloidal Silver Nanoparticles. *Journal of Visualized Experiments* Accepted.

- Adam C. Stahler, Jennifer L. Monahan, Jessica M. Dagher, Joshua D. Baker, Marjorie M. Markopoulos, Diane Iragena, Britney NeJame, Robert Slaughter, Daniel Felker, Larry Burggraf, Zofia E. Gagnon, and Ioana E.P. Sizemore. Following the Abnormal Ossification Process in Tibiotarsi of Developing Chick Embryos Exposed to Sublethal Doses of Platinum Group Metals by Spectroscopic Techniques. Submitted to the *Bone* (June, 2012).

- Piyush J. Shah, Adam C. Stahler, Andrew M. Sarangan, and Ioana E.Pavel Sizemore. Improving the SERS-based Sensing Capabilities of Silver Nanorod Thin Films Through an Oblique Angle Deposition at Cryogenic Temperatures. In Preparation to be submitted to the Journal of Physical Chemistry C.

PRESENTATIONS

Poster Presentation –Ohio Valley Society of Toxicology **September 2010**

- *"Toxicity of platinum group metals in chick embryo tibiotarsi"*

  Marjorie Markopoulos, Jennifer Monahan, Jessica Dagher, Adam Stahler, Tai Lam, Joshua Baker, Britney NeJame, Jacob Cowley, Robert Slaughter, Larry Burggraf, Zofia Gagnon, and Ioana Pavel

  - This presentation was given the Best Master Student Platform Award

Poster Presentation - ACS Dayton Local Poster Session **March 2011**

- *"Spectroscopic investigations of sublethal doses of platinum group metals on chick embryo bone development"*

  Adam Stahler, Marjorie Markopoulos, Jennifer Monahan, Jessica Dagher, Joshua Baker, Tai Lam, Zofia Gagnon, and Ioana Pavel

Oral Presentation - Wright State University's Celebration of Research **April 2011**

- *"Micro-Raman imaging of the bone development in chick embryos exposed to 1.0 ppm sublethal doses of platinum group metals"*

Adam Stahler, Marjorie Markopoulos, Jennifer Monahan, Jessica Dagher, Joshua Baker, Tai Lam, Zofia Gagnon, and Ioana Pavel

Oral Presentation - 2011 ACS Central Region Meeting **June 2011**

- *"Micro-Raman imaging of the bone development in chick embryos exposed to 1.0 ppm sublethal doses of platinum group metals"*

  Adam Stahler, Marjorie Markopoulos, Jennifer Monahan, Jessica Dagher, Joshua Baker, Tai Lam, Zofia Gagnon, and Ioana Pavel

Poster Presentation – Ohio Valley Society of Toxicology **September 2011**

- *"Spectroscopic investigations of the bone development in chick embryos exposed to sublethal doses of platinum group metals"*

  Adam Stahler, Jennifer Monahan, Marjorie Markopoulos, Jessica Dagher, Joshua Baker, Tai Lam, Diane Iragena, Larry Burggraf, Daniel Felker, Zofia Gagnon, and Ioana Pavel

Poster Presentation – 2011 Ohio Inorganic Weekend **October 2011**

- *"Spectroscopic investigations of the bone development in chick embryos exposed to sublethal doses of platinum group metals"*

  Adam Stahler, Jennifer Monahan, Marjorie Markopoulos, Jessica Dagher, Joshua Baker, Tai Lam, Diane Iragena, Larry Burggraf, Daniel Felker, Zofia Gagnon, and Ioana Pavel

Poster Presentation – 2012 ACS Dayton Local Poster session **April 2012**

- *"Improving the SERS-based sensing capabilities of silver nanorod thin films: A SERS study on the effects of fabrication temperature"*

  Adam Stahler, Piyush Shah, Andrew Sarangan, Ioana Pavel Sizemore

    - This poster won the Dayton Local Section Outstanding Poster as a Graduate Student and chosen as an outstanding poster by the Ohio Valley Section of the Society for Applied Spectroscopy.

Oral Presentation - Wright State University's Celebration of Research **April 2012**

- *"Effects of Substrate Temperature on the SERS-based sensing performance of Silver Nanorod Thin Films Fabricated Through Oblique Angle Deposition"*

  Adam Stahler, Piyush Shah, Andrew Sarangan, Ioana Pavel Sizemore

Oral Presentation – 2012 ACS Central Regional Meeting **June 2012**

- *"Improving the SERS-based sensing capabilities of silver nanorod thin films: A SERS study on the effects of fabrication temperature"*

  Piyush J. Shah, Adam C. Stahler, Andrew M. Sarangan, and Ioana E.Pavel Sizemore

Oral Presentation – 2012 ACS Central Regional Meeting **June 2012**

- *"Investigating the abnormal ossification of tibiotarsi of chick embryos exposed to sublethal doses of platinum group metals through micro-Raman spectroscopy"*

  Adam C. Stahler, Jennifer L. Monahan, Jessica M. Dagher, Joshua D. Baker, Marjorie M. Markopoulos, Diane Iragena, Britney NeJame, Robert Slaughter, Daniel Felker, Larry Burggraf, Zofia E. Gagnon, and Ioana E.P. Sizemore

Oral Presentation – 2012 Biennial Conference on Chemical Education **August 2012**

- *"Estimating the SERS enhancement factors of colloidal silver nanoparticles: A laboratory experiment for physical chemistry and nanotechnology courses"*

  Adam C. Stahler, Khadijeh Alnajjar, Joshua Baker, Allie Meyerhoefer, Jennifer Monahan, Ioana Sizemore

Poster Presentation – Fall 2012 ACS National Meeting **August 2012**

- *"Investigating the abnormal ossification of tibiotarsi of chick embryos exposed to sublethal doses of platinum group metals through micro-Raman spectroscopy"*

Adam C. Stahler, Jennifer Monahan, Marjorie Markopoulos, Jessica Dagher, Joshua Baker, Tai Lam, Diane Iragena, Larry Burggraf, Daniel Felker, Zofia Gagnon, and Ioana Sizemore